

https://dspace.org/

Investigating the candidate 5-alpha cluster state in 20Ne at Ex =22.5 MeV with the 22Ne(p,t)20Ne reaction

Baloyi, Lerato Pertunia Lyna

2019

https://hdl.handle.net/10539/27926

Downloaded from a DSpace repository. https://dspace.org/

Investigating the candidate 5-alpha cluster state in ^{20}Ne at $E_x = 22.5$ MeV with the ^{22}Ne(p,t)^{20}Ne reaction

Lerato Pertunia Lyna Baloyi

A dissertation submitted to the Faculty of Science,
University of the Witwatersrand, Johannesburg,
in fulfilment of the requirements for the degree of
Master of Science.

2019

Supervisor:
Dr I. T. Usman, School of Physics, University of the Witwatersrand, Johannesburg.

Co-supervisors:
Prof J. Carter, School of Physics, University of the Witwatersrand, Johannesburg.

Dr R. Neveling, iThemba LABS, Somerset West.

Dr J. A. Swartz, Aarhus University, Denmark.

Declaration

I declare that this dissertation is my own unaided work. It is being submitted for Masters of Science degree to the University of the Witwatersrand, Johannesburg. It has not been submitted previously for any degree or examination to any other university.



Lerato Pertunia Lyna Baloyi
Date: 29 March 2019

Abstract

The ^{20}Ne nucleus was investigated experimentally with a proton beam energy of $E_{\mathrm{p}} = 80$ MeV at zero-degrees scattering angle using the ^{22}Ne(p,t)^{20}Ne reaction. The aim of the project was to investigate if the existence of a state at $E_{\mathrm{x}} = 22.5$ MeV in ^{20}Ne, previously using the same reaction at $E_{\mathrm{p}} = 60$ MeV, can be confirmed. Measurements were performed using the K600 magnetic spectrometer of iThemba LABS and a newly developed gas handling system that ensured constant pressure throughout the experiment for the ^{22}Ne gas target.

In general, a good correspondence between the ^{20}Ne excitation energy spectrum measured in the present experiment and that at $E_{\mathrm{p}} = 60$ MeV was found in the region below 22.5 MeV. Several strongly populated states in ^{20}Ne identified for the previous experiment at $E_{\mathrm{p}} = 60$ MeV were again seen in the present experiment at $E_{\mathrm{p}} = 80$ MeV, for which cross-sections were extracted.

However, with the help of wavelet-based semblance analysis a tentative candidate 5-alpha cluster state at $E_{\mathrm{x}} = 22.5$ MeV, which lies 3.33 MeV above the ^{20}Ne 5-alpha break-up threshold, was established (at $E_{\mathrm{x}} = 22.4$ MeV in this study) to be only weakly populated in comparison to the $E_{\mathrm{p}} = 60$ MeV dataset. The present finding supports the existence of a state at $E_{\mathrm{x}} = 22.4$ MeV but further experimental work is required to investigate its nature.

This work is dedicated to my lovely daughter Mbuyelo Reward Hlungwani and the upcoming little ones.

Acknowledgements

To my supervisor, Dr Iyabo Usman who was always calm in all situations that happened during this research period. Thank you so much Dr for having trust in me when I approached you for the first time, wanting to work with you.

To my co-supervisor at iThemba LABS, Dr Retief Neveling, thank you so much for been the best resource in this research and for never been too busy to help me. More importantely, for sending detailed emails when explaining any concept, irrespective of how small or big the concept is, and also for asking if you have responded to all my emails or you have sent back all the comments. Dr Neveling this is highly acknowledged.

To my project spokesperson and co-supervisor, Dr Jacobus Andreas Swartz who was very helpful in the entire research, when coming to explaination of all the techniques used in this research in comparison with the ones used during his PhD study. Thank you so much for that and also for detailed emails you send and for the skype meetings you arranged with Dr Lindsay Donaldson, trying to explain concepts that I could not understand on email. Dr Swartz this is highly appreciated.

Prof John Carter, my co-supervisor at Wits, who had trust in me towards this research. Thank you so much Prof for the great effort you have contributed to this research, especially on wavelet-analysis, and also for helping me with print out and scan of some figures using your home-printer. This is highly appreciated.

To Prof Paul Papka, thank you so much for designing the gas handling system for this experiment.

Thank you to my fellow Wits Nuclear Structure Research Group, Mr Sunday Olorunfunmi for being helpful and sharing of ideas relating to my MSc research.

Thank you to everyone who helped during data collection of this project.

I would like to acknowledge National Research Foundation and iThemba LABS Top-Up funding for supporting me financially during my research study period.

To my mom, Mavis Mnyamane Mamabolo who always told me to keep on pushing, no matter how hard it was. Thank you so much mommy for the support you have given to me through communicating with cellphone since we are far away from each other.

To my life-partner, Mr Jabulani Aubrey Hlungwani, who supported me with everything during this research period. More importantly, for supporting me verbally when this research was emotionally giving me hard times. Thank you so much for that and also for driving me to Wits during this period so that I can work on the research.

Contents

Declaration ii

Abstract iii

Dedication iv

Acknowledgements v

List of Figures ix

List of Tables xiv

1 Introduction 1

1.1 Cluster states at break-up thresholds 2

1.2 This study 6

2 Theoretical background 9

2.1 DWBA calculations 9

2.1.1 Optical model potential 13

2.1.2 Optical model parameters 15

2.1.3 Angular distribution 16

2.2 Wavelet analysis 17

2.2.1 Formalism of wavelet analysis 17

2.2.2 Continuous Wavelet Transform 18

2.2.3 Wavelet-based semblance analysis 20

3 Experimental method 21

3.1 K600 magnetic spectrometer 21

3.2 K600 focal plane detector package 24

3.2.1 Vertical drift chambers 24

3.2.2 Scintillator detectors 26

3.3 Gas target system 28
3.3.1 Gas handling system 29
3.4 Electronics and DAQ 34
3.4.1 Trigger logic 34
3.4.2 Pre-amplifier cards and TDCs 36
3.4.3 Current integration 36
3.4.4 Data acquisition 36
3.4.5 System dead time measurement 37
3.5 Experimental procedure 37

4 Data analysis, results and discussion **39**
4.1 Particle identification (PID) method 40
4.2 VDC operation 43
4.3 VDC efficiency 45
4.4 TOF offsets 46
4.5 Lineshape correction 48
4.6 Position offsets 51
4.7 Energy calibration procedure 53
4.8 Background subtraction 56
4.9 Experimental cross-sections 60
4.10 Comparison of $E_{\mathrm{p}} = 80$ and $E_{\mathrm{p}} = 60$ MeV data 64
4.11 Discussion 68

5 Conclusions and future work **70**
5.1 Conclusions 70
5.2 Future work 71

References **72**

List of Figures

1.1 Diagram indicating the threshold energies (in MeV) of the different α-decay modes in the four lightest self-conjugate α-nuclei, known as the Ikeda diagram [Ike68]. 2

1.2 The 0^+ states in ^{20}Ne. State at $E_x = 22.5$ MeV which is represented by a blue arrow is not yet confirmed as a 0^+ (taken with permission from [Swa15]). 6

2.1 Shape of the angular distribution predictions for the first 0^+ (ground state), 2^+ and 4^+ states from the ^{22}Ne(p,t)^{20}Ne reaction with a proton beam energy of $E_p = 80$ MeV, obtained from the DWUCK4 calculation. 16

3.1 The iThemba LABS Separated Sector Cyclotron (SSC) facility. . 22

3.2 The K600 magnetic spectrometer layout for measurements at zero degrees with detectors in the medium dispersion focal plane. The L-shape beamstop was replaced with a smaller beamstop in this experiment (taken with permission from[Nev17]). 23

3.3 The focal plane detector package employed during the data collection period for the present experiment. The charged particles exit the K600 vacuum chamber and move through the detectors from left to right. The first detector on the left is the VDC1, followed by the first and second scintillators to the right of it. 25

3.4 A drawing of 10 mm thick gas target cell. 29

3.5 The target ladder with two gas cells at the top. 30

3.6 A schematic of the target gas cell gas handling system. 31

3.7 The target gas cell gas handling system. 33

3.8 Graph showing gas pressure and flow rate with respect to time. 34

3.9 The trigger electronics diagram. 35

3.10 The zero degree beamstop placed between dipole magnets. . . . 38

4.1 (a): A scatterplot of the energy deposited in the scintillator versus TOF for the empty target. (b): A scatterplot of the energy deposited in the scintillator versus TOF for the ^{22}Ne(p,t)^{20}Ne reaction with a 56.3 MeV (p,t) field setting. The black rectangle indicates tritons (particle of interest), the black circle indicates deuterons. The rest represent beam-related background as shown in the top plot. 41

4.2 Measured position spectrum for the ^{22}Ne(p,t) reaction, without a PID gate as shown in Fig. 4.1. The peak on the left is deuterons whereas the peak on the right is tritons. 42

4.3 Measured position spectrum for the ^{22}Ne(p,t) reaction with a PID gate as shown in Fig. 4.1. 42

4.4 The drift time spectrum for the tritons measured in the X-wire chamber. 44

4.5 The lookup table. 44

4.6 The drift distance spectrum corresponding to the drift time spectrum in Fig. 4.4. 45

4.7 The number of signal wire hits per event for VDC X1. 46

4.8 A typical TOF spectrum with the peak representing the tritons centered around 225 ns. A Gaussian was fitted to this peak, as shown in red. 47

4.9 A scatterplot of the TOF vs X1 position for the ^{22}Ne(p,t) reaction at zero degrees, without line shape correction. 49

4.10 A scatterplot of the TOF vs X1 position for the ^{22}Ne(p,t) reaction at zero degrees, with line shape correction. 49

4.11 Measured X1 position spectrum, without line shape correction. . 50

4.12 The X1 position spectrum, with line shape correction. 50

4.13 PID selected position spectrum for the ^{22}Ne(p,t) reaction for runs 2142 - 2157 without taking position offsets into account. . . 52

4.14 PID selected position spectrum for the ^{22}Ne(p,t) reaction for runs 2142 - 2157 with position offsets taken into account. 52

4.15 Focal plane position spectrum for the ^{22}Ne gas target showing three states of ^{10}C and the 16.73 MeV ^{20}Ne state. 54

4.16 Focal plane position spectrum for the aramid showing ^{10}C states. 54

4.17 The second order polynomial relationship between rigidity and peak position obtained when using ^{10}C states and one ^{20}Ne state. 55

4.18 The excitation energy spectrum for the background data at zero degrees. The green spectrum is the background data plot for the back foil, whereas the blue one is the plot for the front foil. The red spectrum is the sum of back and front foil. 57

4.19 Different scenarios of the ^{12}C(p,t)^{10}C reaction with either protons or tritons moving through ^{22}Ne gas. 58

4.20 Double peaking effect for the case of the ground state of ^{10}C. The green peak represents the back foil scenario whereas the blue one represents the front foil scenario. 58

4.21 The excitation energy spectrum for the ^{22}Ne(p,t) reaction at zero degrees. The red spectrum is the ^{22}Ne gas spectrum, and the green one is the sum of the background data. The blue spectrum is the background subtracted spectrum. 59

4.22 Aramid subtracted excitation energy spectrum showing observed states (labeled) in ^{20}Ne. 60

4.23 An example of how the peaks were fitted using Gaussian (green colour) on the ^{22}Ne gas target data before background subtraction. 63

4.24 An example of how the peaks were fitted using Gaussian (green colour) on the ^{22}Ne gas target data after background subtraction. 63

4.25 Excitation energy spectrum for the ^{22}Ne(p,t)^{20}Ne reaction at $E_{\mathrm{p}} = 60$ MeV (taken with permission from [Swa15]). 66

4.26 Comparison of present data at $E_{\mathrm{p}} = 80$ MeV with data from [Swa15] at $E_{\mathrm{p}} = 60$ MeV for the ^{22}Ne(p,t)^{20}Ne reaction. The blue spectrum represents the excitation energy spectrum for the present data and the red spectrum represents the excitation energy spectrum for the $E_{\mathrm{p}} = 60$ MeV data. The vertical dashed lines indicate the region of interest. 66

4.27 (a) Excitation energy spectrum for the present data, and (b) its two-dimensional wavelet coefficient plot. (c) Excitation energy spectrum for the $E_{\mathrm{p}} = 60$ MeV data, and (d) its two-dimensional wavelet coefficient plot. Red and blue in the two-dimensional wavelet coefficient plots represent positive and negative scale values, respectively. (e) Semblance plot of comparison of b and d showing the correlation between the two data sets. (f) Semblance plot projection for the region around $E_{\mathrm{x}} = 22.5$ MeV which is the region of interest. 67

List of Tables

2.1 Optical model parameters used for DWBA calculation (taken from [Ols73]). 15

3.1 The TOF ranges of tritons, deuterons and protons at triton energy setting. 28

3.2 Chemical purity of the ^{22}Ne gas bottle used. 32

4.1 TOF offsets for all the runs with respect to Ne run 2142, the reference run. 48

4.2 Position offsets for all the runs with respect to Ne run 2142, the reference run. 53

4.3 States selected for energy calibration. The value 5.30 MeV represents the average of the 5.22 MeV and 5.38 MeV ^{10}C states. 55

4.4 Cross sections and widths (FWHM) for the states observed in ^{20}Ne in Fig. 4.22. 62

4.5 Comparison of cross-sections ($\frac{d\sigma}{d\Omega}$) for the states observed in ^{20}Ne above $E_{\mathrm{x}} = 21$ MeV at $E_{\mathrm{p}} = 80$ MeV and $E_{\mathrm{p}} = 60$ MeV. Data(80) represents the present data and Data(60) represents the data used in Ref. [Swa15]. 65

Chapter 1

Introduction

The study of nuclear clustering began with the discovery of α radiation by Rutherford, and the development of quantum mechanics. The α-particle was described as undergoing quantum-mechanical tunneling from inside the decaying nucleus [Gam28]. A decade later, after the discovery of the proton and neutron as constituents of nuclei, the resonating group method was developed. This describes α-particles as clusters while allowing protons and neutrons to maintain their fermionic quantum statistics [Whe37].

The work of Hafstad and Teller can be considered to be the first in the field of alpha clustering in nuclear physics. They described even-even $N = Z$ nuclei in terms of an alpha particle model with bonds connecting the clusters. The model first considered the interaction of two neutrons with two protons, and then the interaction between groups of particles. Over the years alpha clustering became known as a phenomenon that explains the existence of specific excited states in nuclei which cannot be described within the nuclear shell model. The so-called Ikeda diagram [Ike68], a portion of which is shown in Fig. 1.1, lists the alpha break-up threshold energies around which alpha-cluster states in self-conjugate alpha nuclei can be expected to exist.

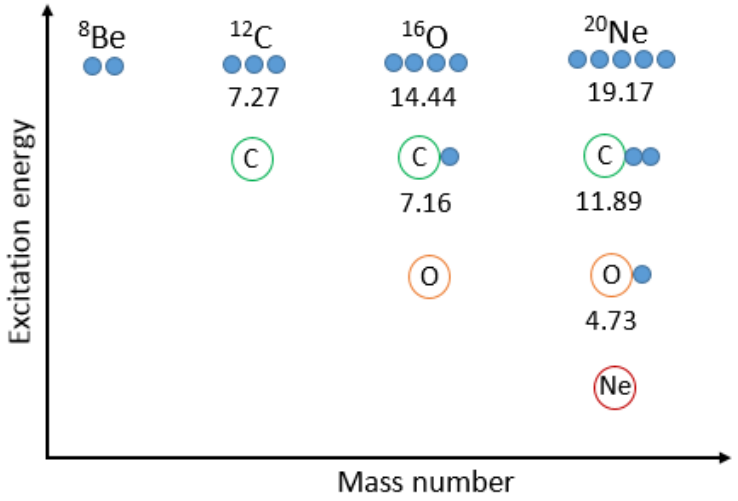

Figure 1.1: Diagram indicating the threshold energies (in MeV) of the different α-decay modes in the four lightest self-conjugate α-nuclei, known as the Ikeda diagram [Ike68].

1.1 Cluster states at break-up thresholds

The existence of excited states that represents an N-alpha cluster structure can be seen in the Ikeda diagram on Fig. 1.1. For example, for ^{8}Be a cluster structure is expected in its ground state and for ^{12}C and ^{16}O such a state is expected close to 7.27 MeV and 14.44 MeV, respectively. Ikeda *et al.* [Ike68] predicted that the 5-α 'Hoyle-like' cluster state in ^{20}Ne may exist in the excitation energy region near the 5-α breakup threshold (E_{x} = 19.17 MeV).

A number of experiments were conducted in order to investigate cluster states in different light nuclei (such as ^{8}Be, ^{12}C and ^{16}O). The ^{8}Be nucleus is unstable in nature, and has a very low Q_{α} value. Its ground state has been studied and understood as a 2α-clustering state by using the α-cluster model in the low excitation energy region [Hor12, Yam10]. In a study by Myo *et al.* [Myo14] it was found, using a tensor-optimized shell model, that the tensor contributions of the ground state are stronger than the ones for highly excited states. It was determined that the kinetic energies and the central contributions of the ground state are almost twice that of the ^{4}He values. These features suggest 2α-clustering for the ground state of ^{8}Be. The cluster structure of the ^{8}Be ground state is essential for nucleosynthesis of ^{12}C in stars [Myo14].

The ^{12}C nucleus is created in the fusion of three α-particles through the formation of the short-lived ^{8}Be ground state as an intermediate state [Sal52]. In 1954, Hoyle postulated the existence of a 0^+ excited state at $E_x = 7.65$ MeV in ^{12}C [Hoy54]. Hence, it is called the Hoyle state. This state was experimentally confirmed to exist by Cook *et al.* [Coo57]. Its energy could not be reproduced by shell model calculations [Kar95]. The Hoyle state plays an important role as a prototype of α-cluster states in light nuclei. In some theories it is predicted to be a dilute self-bound gas of bosonic α-particles, similar to a Bose-Einstein Condensate (BEC) [Toh01, Fun03, Yam04, Fun05, Yam05, Fun06].

The Hoyle state provides the gateway for the synthesis of all elements from itself to the heaviest elements occurring naturally [Fyn05]. It lies 375 keV above the 3α-decay threshold [Fre09], and it was found experimentally from inelastic electron scattering data that its volume is 3.4 times larger than that of the ground state [Nak71]. This larger volume may allow α-particles to obtain their quasi-free characteristics in something approaching an α-particle gas or maybe a bosonic condensate [Toh01]. Its dilute density with a large spatial extension was also found using electron scattering in a study by Chernykh *et al.* [Che07]. These results were compared with calculations using a charge form-factor with the predictions of different theoretical models, which include fermionic molecular dynamics (FMD) [Rot04], α-clustering and the BEC. The α-cluster results agreed very well with the BEC approach and also with resonating group method calculations [Kam81].

One way to learn more of the structural properties of the Hoyle state experimentally, is to find the location of its collective (2^+) excitation state. If this 3α cluster state were arranged in a linear form (3α chain) it would then have a 2^+ excitation at 0.8 MeV above the 0^+ Hoyle state [Mer92]. In the study of Freer *et al.* [Fre09], the result showing the existence of a 2^+ excitation of the Hoyle state was presented and it was found at about 2 MeV above the 0^+ Hoyle state.

A potential 4α-cluster candidate (0^+_6) in ^{16}O is located at $E_x = 15.097(5)$ MeV, which is above the 4α-particle breakup threshold at $E_x = 14.437$ MeV. It was identified as a candidate by Funaki *et al.* [Fun08] through solving the four-

body equation of motion based on the orthogonality condition model. Below the breakup threshold, which is at $E_{\rm x} = 14.437$ MeV there are two 0^+ states (0^+_4 and 0^+_5) at $E_{\rm x} = 13.6(1)$ and $E_{\rm x} = 14.032(15)$ MeV, respectively. The candidate 0^+_5 is known to be strongly excited via monopole transitions from the ground state [Fun07, Li17].

The state at $E_{\rm x} = 15.097(5)$ MeV [Cen16] is 0.66 MeV above the 4α-particle breakup threshold, and calculations predict that it has a large radius of 5.0 fm that could indicate a dilute density structure. The results from an $\alpha + {}^{12}$C elastic and inelastic scattering study [Ohk10] suggest that the 0^+_6 state could be a good candidate for the 4α cluster condensate state since its moment of inertia is drastically reduced as compared to other states. This statement is also supported by the calculations performed with the Tohsaki-Horiuchi-Schuck-Röpke (THSR) α-cluster wave function [Fun10], with an estimated width of 34.0 keV [Fun09].

The ^{20}Ne nucleus has been investigated experimentally and theoretically from the cluster point of view [Hor68, Swa15] and its 5-alpha condensate state is like the condensate states in ^{8}Be, ^{12}C and ^{16}O. As an example, the two-channel "α-cluster plus ^{16}O model" where the clusters are in the ground state or in the quadrupole-type excited states, was applied to the ^{20}Ne nucleus [Ban76]. It was found that α-clustering enhances the $B(E2)$ values to about two-thirds of the observed magnitude.

In the past, a lot of attention has been given to molecular aspects and α-correlations in light nuclei. As an example, the ^{20}Ne nucleus has been investigated extensively on the molecular aspects and alpha-correlations [Dav63, Tan74]. It was clarified that the first $K^\pi = 0^-$ rotational band built on the 5.79 MeV level has dominantly α-correlated properties with a molecule-like ^{16}O + α conjugation [Mat75]. It was also shown that the $K^\pi = 0^+$ ground state band with spin up to $8\hbar$ has certain transient properties changing from the molecule-like structure to a shell-like structure or vice versa [Mat75].

In the study of Bando [Ban76], the α-clustering structure of ^{20}Ne was investigated using the Resonating Group Method (RGM) for the ^{16}O + α system. This was performed by calculating the ^{16}O − α scattering phase

shifts for $0 \leq L \leq 14$, and alpha-decay widths etc. It was found using scattering phase shifts that the $K^{\pi} = 0^{+}$ ground state band of ^{20}Ne is composed of states with spin values up to $8\hbar$, while there appears an excited $K^{\pi} = 0^{+}$ band with spin values of up to $12\hbar$. The resonance states ($L \leq 10$) are considered to involve much of the (12,0)SU_3 and more-excited (λ,0) configuration in the internal region.

The ^{20}Ne nucleus is well suited to form α-clusters. This is because it exists as an axially-symmetric quadrupole ellipsoid at equilibrium [Spe81], and this deformation causes degeneracy around shell closures, which are capable of forming α-clusters [Ebr12]. In the study of Yamada *et al.* [Yam04], the Hill-Wheeler equation was applied to the 5α condensate model, and a tentative 5α-cluster state was predicted at $E_{\mathrm{x}} = 22.14$ MeV. In the experimental study of Swartz *et al.* [Swa14], a tentative 5α-cluster state, which could not be accounted for by the shell model calculations, was observed at $E_{\mathrm{x}} = 22.5$ MeV.

Experimentally, the ^{20}Ne nucleus was investigated in the study by Swartz *et al.* [Swa15] with $E_{\mathrm{p}} = 60$ MeV in the energy region from $E_{\mathrm{x}} = 17$ MeV to $E_{\mathrm{x}} = 23$ MeV using the ^{22}Ne(p,t)^{20}Ne reaction. It was performed over a range of reaction scattering angles including zero degrees using the (p,t) reaction with high energy-resolution of 40 keV. Six new states, namely at $E_{\mathrm{x}} = 17.67$ MeV, 18.84 MeV, 20.59 MeV, 21.16 MeV, 21.80 MeV and 22.5 MeV were discovered with spins and parities 2^{+}, $0^{+}/1^{-}$, $1^{-}/2^{+}$, 0^{+}, 1^{-} and (0^{+}), respectively. The states at 20.59 MeV, 21.16 MeV and 21.80 MeV were suggested to be the $T = 2$ isobaric analogue states (IAS). All these states except the state at 22.5 MeV were accounted for by shell-model calculations within the $1s0d$, $2\hbar w$ and $1\hbar w$ as shown in Fig. 1.2 [Swa15]. The state at $E_{\mathrm{x}} = 22.5$ MeV was assumed to be the candidate for the 5α-cluster state. However, this state was difficult to isolate as it was situated on a background consisting of the $E_{\mathrm{x}} = 10.89$ MeV state of ^{14}O from the ^{16}O(p,t)^{14}O reaction on the aramid foil [Swa15].

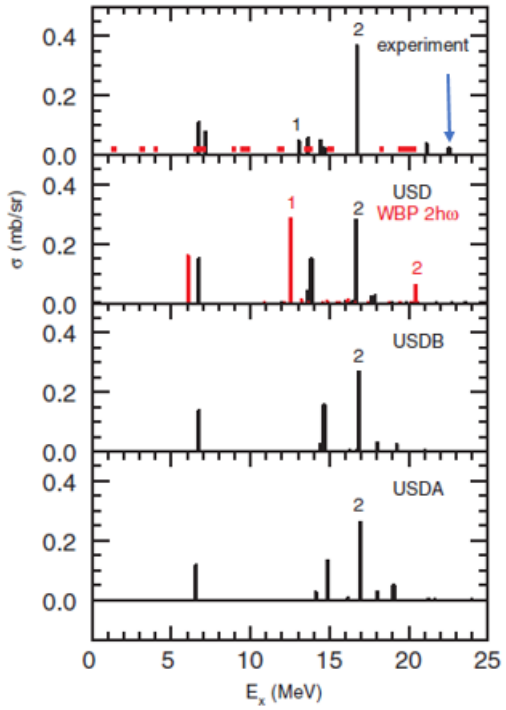

Figure 1.2: The 0^+ states in ^{20}Ne. State at $E_x = 22.5$ MeV which is represented by a blue arrow is not yet confirmed as a 0^+ (taken with permission from [Swa15]).

1.2 This study

In order to understand the background of the present experiment, a new experiment [Swa17] was proposed, following up on the ^{22}Ne(p,t)^{20}Ne study from Swartz *et al.* [Swa15], to perform a measurement of the ^{22}Ne(p,^{3}He)^{20}F reaction in order to see whether the three $T = 2$ states are reproduced in the isobaric nucleus. Finding in ^{20}F the Isobaric Analogue States (IAS) of the states measured at 20.59 MeV, 21.16 MeV and 21.80 MeV in ^{20}Ne, would serve as confirmation of the $T = 2$ character of these states. The experiment was performed at higher energies to ensure that the ^{3}He particles would reach the focal plane trigger detectors, making the measurement possible (keeping in mind that the doubly charged ^{3}He has a smaller range in material than tritons). In addition, not finding any IAS for the 22.5 MeV state of ^{20}Ne in ^{20}F could support the notion that the 22.5 MeV state has a $T = 0$ character, which would be in support of this state's candidacy as a 5α candidate.

To properly compare the (p,t) and (p,^{3}He) results for the three states at

20.59 MeV, 21.16 MeV and 21.80 MeV, new (p,t) measurements at 80 MeV were necessary to allow comparison of the angular distributions of these states observed with different reactions at the same incident beam energies. As a result of these measurements data for the 22.5 MeV excitation energy region in ^{20}Ne became available from measurements of the ^{22}Ne(p,t)^{20}Ne reaction at $E_{\mathrm{p}} = 80$ MeV. While this was not the main aim of the proposal by Swartz *et al.* [Swa17], the analysis of the zero degree data for the ^{22}Ne(p,t)^{20}Ne reaction at $E_{\mathrm{p}} = 80$ MeV will be the focus of this dissertation.

This measurement is indeed not optimally designed to observe the 0^+ state seen by Swartz *et al.* [Swa15] at 22.5 MeV, since the cross section for the (p,t) reaction is expected to be smaller at $E_{\mathrm{p}} = 80$ MeV than with $E_{\mathrm{p}} = 60$ MeV. This is because the angular momentum that the higher energy projectiles can impart on the target is higher and it is more likely to excite states with higher angular momentum. However, there are two advantages of analyzing the available data at 80 MeV. In the $E_{\mathrm{p}} = 60$ MeV experiment, the specific setting of the K600 fields caused the 22.5 MeV state to be very close to the edge of the focal plane, making background subtraction less optimal. In the new experiment the observed excitation energy region was chosen such that the 22.5 MeV region is not on the edge of energy acceptance. Secondly, the different beam energy means a slight shift in the position of the background peaks from the aramid gas cell windows relative the 22.5 MeV region in ^{20}Ne, which was problematic in the $E_{\mathrm{p}} = 60$ MeV measurement.

This dissertation, therefore, focuses on a subsection of a bigger project, which is to see whether the state at $E_{\mathrm{x}} = 22.5$ MeV is reproduced in another study or not using the ^{22}Ne(p,t)^{20}Ne reaction at zero degrees and to see how its cross section changes at a higher beam energy. It is expected that the cross section for populating this state would be smaller. However, despite the lower cross-section, the availability of semblance analysis will make it possible to test whether the weak structure seen at 80 MeV is the 22.5 MeV state in ^{20}Ne as observed in the $E_{\mathrm{p}} = 60$ MeV experiment.

The layout of this dissertation is as follows:

Chapter 1 gives an introduction about alpha clustering and a motivation for

the present study.

Chapter 2 describes the theoretical background which includes the Distorted Wave Born Approximation (DWBA) calculations, and the wavelet analysis technique called wavelet-based semblance analysis which will be used to compare two excitation energy spectra.

Chapter 3 describes the experimental method which includes the equipment used for this study as well as the data acquisition procedure.

Chapter 4 outlines the analysis of the data, presentation of the results and discussion.

Chapter 5 presents a conclusion of this study, as well as an overview of the proposed future work.

Chapter 2

Theoretical background

In this chapter, the appropriate theoretical considerations for this study are outlined. This includes Distorted Wave Born Approximation (DWBA) calculations, and the use of the wavelet analysis technique.

2.1 DWBA calculations

The strength with which a specific state will be populated by one or two-step direct-transfer nuclear reactions can be predicted by the Distorted Wave Born Approximation (DWBA) theory. This is done specifically for a certain scattering angle and beam particle energy. This theory treats the projectile and ejectile ions in a transfer nuclear reaction as moving under the influence of long-range Coulomb and short-range nuclear forces. Elastic scattering is assumed to be the important component of a transfer reaction, and the inelastic component is treated as a perturbation. The transfer reaction used in the present study ^{22}Ne(p,t)^{20}Ne allows energy, momentum and angular momentum to be exchanged by the projectile and the target nucleus. It also allows a transfer of mass that produces a fundamental change in the description of the reaction from the one used for inelastic scattering. As an example, if $\overrightarrow{P}_{\mathrm{p}}$ is the incident proton momentum and $\overrightarrow{P}_{\mathrm{t}}$ is the momentum of the emerging triton, then the momentum $\overrightarrow{P}$ transferred to the target nucleus by the transfer of the neutron to the nucleus is given by conservation of momentum as

$$\overrightarrow{P} = \overrightarrow{P}_{\mathrm{p}} - \overrightarrow{P}_{\mathrm{t}}. \tag{2.1}$$

Semiclassically, the orbital angular momentum transfer simulates the effects on the proton and triton waves of strong absorption in the nuclear interior. If the bound-state radial function $U(r)$ falls rapidly with r then it is expected that

$$\frac{d\sigma}{d\Omega} \propto |j_l(|\overrightarrow{P}_{\mathrm{p}} - \overrightarrow{P}_{\mathrm{t}}|r_0)|^2. \tag{2.2}$$

This equation has oscillations as a function of momentum transfer and for zero angular momentum transfer ($l = 0$), there is a peak at zero degrees. The peak falls off inside $P \sim \frac{\pi}{r_0}$. The cross section disappears for higher angular momenta ($l = 1, 2, ...$) at zero degrees and peaks further out at a position depending on the l-value. The orbital angular momentum $\triangle l$ transferred to the nucleus may be calculated from the orbital quantum numbers and it restrains the position at which the transfer took place according to

$$\triangle l \sim |\overrightarrow{P} \times \overrightarrow{r}| = |(\overrightarrow{P}_{\mathrm{p}} - \overrightarrow{P}_{\mathrm{t}}) \times \overrightarrow{r}| \tag{2.3}$$

and

$$\frac{d\sigma}{d\Omega} \propto |\int_{r_0}^{\infty} r dr j_l(|\overrightarrow{P}_{\mathrm{p}} - \overrightarrow{P}_{\mathrm{t}}|r)U(r)|^2. \tag{2.4}$$

DWBA calculations for the ^{22}Ne(p,t)^{20}Ne reaction were performed using DWUCK4 which in general calculates the scattering and reaction observables for binary nuclear reactions. These calculations were performed using a zero-range interaction [Kun13].

The cross section of any reaction of the form A(a,b)B, in DWBA may be written as [Sat83]

$$\frac{d\sigma}{d\Omega} = \frac{\mu}{2\pi h^2}\frac{v_\mathrm{b}}{v_\mathrm{a}}\frac{1}{(2J_\mathrm{A}+1)(2s_\mathrm{a}-1)}\Sigma_{M_\mathrm{A}M_\mathrm{B}m_\mathrm{a}m_\mathrm{b}}|T^{M_\mathrm{A}M_\mathrm{B}m_\mathrm{a}m_\mathrm{b}}|^2, \tag{2.5}$$

where μ is the reduced mass of the whole system, J_A is the total angular momentum of the target nucleus, s_a is the spin of the projectile, v_a and v_b are the projectile and ejectile speeds, and M_A, M_B, m_a and m_b are the masses of the target nucleus, residual nucleus, projectile and ejectile, respectively.

The DWUCK4 code calculates a transition amplitude T for a reaction of the form A(a,b)B as follows [Sat83]:

$$T = \vartheta \int d^3r_\mathrm{b} \int d^3r_\mathrm{a} X^{(-)*}(\overrightarrow{k}_\mathrm{f}, \overrightarrow{r_\mathrm{b}})\langle \mathrm{Bb}|V|\mathrm{aA}\rangle X^{(+)}(\overrightarrow{k}_\mathrm{i}, \overrightarrow{r_\mathrm{a}}), \tag{2.6}$$

where the variable ϑ is the Jacobian for the transformation of coordinates from the laboratory to the centre-of-mass frame for the (a,A) and (b,B) systems. $X^{(-)}$ and $X^{(+)}$ are the distorted waves, and $\overrightarrow{r_\mathrm{a}}$ and $\overrightarrow{r_\mathrm{b}}$ are the relative coordinates for the systems (a,A) and (b,B), respectively. The momenta of the incoming and outgoing spherical plane waves are represented by the variables $\overrightarrow{k}_\mathrm{i}$ and $\overrightarrow{k}_\mathrm{f}$. The expression $\langle \mathrm{Bb}|V|\mathrm{aA}\rangle$ is the form factor for the reaction, and it must contain a δ function between the coordinates $\overrightarrow{r_\mathrm{a}}$ and $\overrightarrow{r_\mathrm{b}}$ in order to satisfy the zero-range approximation [Kun13].

A plane wave of momentum $\overrightarrow{k}$ together with an outgoing or incoming spherical scattered wave is asymptotically described by the distorted waves $X^{(\pm)}(\overrightarrow{k}, \overrightarrow{r})$ [Kun93]. In case of no Coulomb potential it has the form

$$X^{(\pm)}(\overrightarrow{k}, \overrightarrow{r}) \rightarrow e^{ikr} + f(\theta)\frac{e^{ikr}}{r}. \tag{2.7}$$

The final distorted waves with an incoming scattered wave condition is related to the solution with the outgoing waves by

$$X^{(-)*}(\overrightarrow{k}, \overrightarrow{r}) = X^{(+)}(-\overrightarrow{k}, \overrightarrow{r}). \tag{2.8}$$

The distorted waves are matrices in spin space when the initial and final projectiles have spin,

$$X^{(\pm)}(\overrightarrow{k},\overrightarrow{r})\eta_{\mathrm{s,m}} = \sum_{m'} X^{(\pm)}_{m,m'}(\overrightarrow{k},\overrightarrow{r})\eta_{s,m'}, \tag{2.9}$$

where the $\eta_{\mathrm{s,m}}$ are the spin functions and $X^{(\pm)}_{m,m'}(\overrightarrow{k},\overrightarrow{r})$ is given by

$$X^{(\pm)}_{m,m'}(\overrightarrow{k},\overrightarrow{r}) = \frac{\sqrt{4\pi}}{kr}\sum_{J,L} i^L\sqrt{2L+1}X_{JLs}(kr)(LsMm|JM') \times (LsM'-m'm'|JM')Y_L^{M'-m'}(\widehat{r})d^L_{0,M'-m'}(\widehat{k}), \tag{2.10}$$

where $d^L_{0,\mathrm{m}}$ is the rotation function for integer spin.

The radial part of the distorted waves satisfies the equation

$$\left\{\frac{d^2}{dr^2} + k^2 - \frac{L(L+1)}{r^2} - \frac{2\mu}{\hbar^2}[V(r) + V_{\mathrm{C}}(r) + V_{\mathrm{so}}(r)\overrightarrow{L}.\overrightarrow{s}\right\} X_{JLs}(kr) = 0. \tag{2.11}$$

where $V(r)$ is a central potential with real and imaginary parts, $V_{\mathrm{C}}(r)$ is a Coulomb potential for a uniform charge distribution of radius R_{C} and $V_{\mathrm{so}}(r)$ is a spin-orbit potential.

The radial functions $X_{JLs}(kr)$ satisfy the boundary conditions $X_{JLs}(k0) = 0$ at the origin and they are given by

$$X_{JLs}(kr) \to \frac{i}{2}[H^-_L(kr) - \eta^J_L H^+_L(kr)]e^{i\sigma L}. \tag{2.12}$$

2.1.1 Optical model potential

The interaction of nuclei in the presence of the strong nuclear force is described by the optical model potential [Sat80]. The interaction of the nucleons is replaced by a two-body interaction $V(r)$ between the incident projectile and the target nucleus [Hod78] and is given by

$$V(r) = V_{\mathrm{C}}(r) + iV_{\mathrm{N}}(r), \tag{2.13}$$

where $V_{\mathrm{C}}(r)$ is the Coulomb potential due to a uniformly charged sphere and $V_{\mathrm{N}}(r)$ is the nuclear scattering potential.

Nuclear scattering is represented by the optical model potential in terms of a complex potential $V_{\mathrm{N}}(r)$. Mathematically it is written as follows:

$$V_{\mathrm{N}}(r) = V_{\mathrm{R}}(r) + iW(r), \tag{2.14}$$

where $V_{\mathrm{R}}(r)$ is the real part of the potential and is related to elastic scattering, whereas $W(r)$ is the imaginary part and it accounts for absorption, and r represents the radial distance.

In the present project, the optical model potential used is the combination of a Woods-Saxon volume and surface derivatives. The volume Wood-Saxon potential and its derivatives or surface Wood-Saxon potentials with real ($V_{\mathrm{R}}(r)$) and imaginary ($W(r)$) parts are as follows [Kun13]

Volume Wood-Saxon potential:

$$V(r) = V_{\mathrm{R}} f(x_{\mathrm{R}}) + iW f(x_{\mathrm{I}}), \tag{2.15}$$

where

$$f(x_{\mathrm{i}}) = \frac{1}{[1 + exp(x_{\mathrm{i}})]}. \tag{2.16}$$

Derivative potential or surface Wood-Saxon potential:

$$V(r) = V_{\mathrm{R}} g(x_{\mathrm{R}}) + iW g(x_{\mathrm{I}}), \tag{2.17}$$

where

$$g(x_{\mathrm{i}}) = \frac{df(x_{\mathrm{i}})}{dx}. \tag{2.18}$$

Second derivative Wood-Saxon potential:

$$V(r) = V_{\mathrm{R}} h(x_{\mathrm{R}}) + iW h(x_{\mathrm{I}}), \tag{2.19}$$

where

$$h(x_{\mathrm{i}}) = \frac{d^2 f(x_{\mathrm{i}})}{dx^2}. \tag{2.20}$$

The spin-orbit potential from a volume and surface Wood-Saxon are expressed respectively as [Kun13]

$$V_{\mathrm{so}}(r) = \left(-V_{\mathrm{R}} \frac{1}{r} \frac{df(x_{\mathrm{R}})}{dr} - iW \frac{1}{r} \frac{df(x_{\mathrm{I}})}{dr} \right) L.s, \tag{2.21}$$

$$V_{\mathrm{so}}(r) = \left(-V_{\mathrm{R}} \frac{1}{r} \frac{dg(x_{\mathrm{R}})}{dr} - iW \frac{1}{r} \frac{dg(x_{\mathrm{I}})}{dr} \right) L.s, \tag{2.22}$$

The real part is generally written as

$$V(r) = V_{\mathrm{Rc}}(r) + V_{\mathrm{so}}(r) + V_{\mathrm{rC}}(r) + V_{\mathrm{RC}}(r), \tag{2.23}$$

where V_{Rc} is the central real part, V_{so} is the spin-orbit contribution, V_{rC} represents the Coulomb contribution at $r \leq R_{\mathrm{C}}$, and V_{RC} is the Coulomb contribution at $r \geq R_{\mathrm{C}}$ (R_{C} is the Coulomb radius). The imaginary part is written as:

$$W(r) = W_{\mathrm{V}}(r) + W_{\mathrm{S}}(r), \tag{2.24}$$

where W_{V} is the imaginary volume and W_{S} is the imaginary surface term. The radius R is determined using the equation $R = r_{\mathrm{o}}A^{1/3}$ where r_{o} is a constant and it relates to angular momentum transfer (l) by $l \leqslant dPR$ where dP is the momentum difference between the proton and the triton.

2.1.2 Optical model parameters

The accuracy of the DWBA calculations depend on the chosen values for the optical model parameters V_{R}, r_{R}, a_{R}, W_{V}, W_{S}, r_{W}, a_{W} and r_{C} and they represent the real potential, real part radius, real part diffuseness, imaginary volume, imaginary surface, imaginary part radius, imaginary part diffuseness and Coulomb radius, respectively. Table 2.1 shows a list of the optical model parameters which were used in the present DWBA calculations. These parameters were chosen by Olsen *et al.* [Ols73] for $E_{\mathrm{p}} = 40$ MeV not $E_{\mathrm{p}} = 80$ MeV. These optical model parameters were also used for the $E_{\mathrm{p}} = 60$ MeV data [Swa15]. The angular maxima for the DWBA results for the $E_{\mathrm{p}} = 60$ MeV and the actual $E_{\mathrm{p}} = 60$ MeV data match well. This indicates that the angular distribution are not that sensitive to changes in the optical model parameters, although it is important to choose the correct beam energy.

Table 2.1: Optical model parameters used for DWBA calculation (taken from [Ols73]).

Channel	V_{R} (MeV)	r_{R} (fm)	a_{R} (fm)	W_{V} (MeV)	W_{S} (MeV)	r_{W} (fm)	a_{W} (fm)	r_{C} (fm)
p+^{22}Ne	52.2	1.11	0.57	6.2	8.2	1.11	0.50	1.11
t+^{20}Ne	160.4	1.20	0.72	25.0	0.0	1.40	0.84	1.30

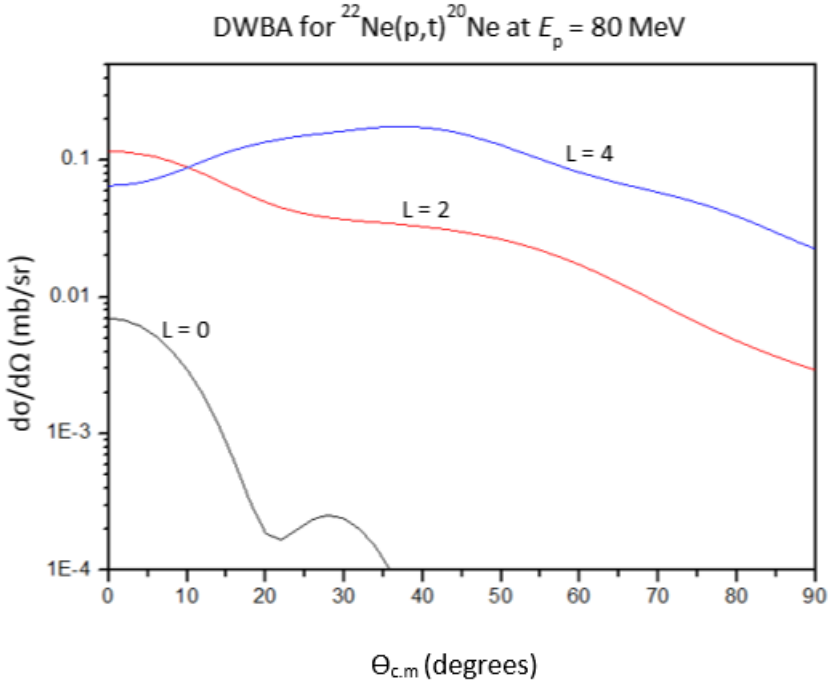

Figure 2.1: Shape of the angular distribution predictions for the first 0^+ (ground state), 2^+ and 4^+ states from the ^{22}Ne(p,t)^{20}Ne reaction with a proton beam energy of $E_\mathrm{p} = 80$ MeV, obtained from the DWUCK4 calculation.

2.1.3 Angular distribution

The DWUCK4 code was used to perform calculations for the first three states of ^{20}Ne, which are 0^+ (ground state), 2^+ (1.633 MeV) and 4^+ (4.247 MeV) from the ^{22}Ne(p,t)^{20}Ne reaction, with a proton beam energy of $E_\mathrm{p} = 80$ MeV. This beam energy allowed excitation energies up to about 24 MeV to be measured. The zero-range force constant from Ref. [Ols73] ($D_0^2 = 26.2 \times 10^4$ MeV^2 fm^3) was used for these calculations to generate the absolute cross-section values shown in Fig. 2.1, the angular distribution spectrum. The results obtained are not very sensitive to the optical model parameters used, hence the optical model values in Ref. [Ols73] for the incoming and outgoing channels were employed for this calculation.

Figure 2.1 shows that a 0^+ ground state would have a maximum at zero degrees. From experimental evidence [Swa14], we also know however that the 16.73 MeV 0^+ state in ^{20}Ne follows almost exactly the same angular distribution as the 0^+ ground state when populated by ^{22}Ne(p,t)^{20}Ne. Based on that, it is likely that

a 0^+ state above 20 MeV in ^{20}Ne, such as the proposed 5-alpha cluster state, would follow a similar distribution trend as well. Therefore, it is expected that this scenario is true for 2^+ and 4^+ states, whereas the absolute values are not expected to be the same. The second maximum is found around 28.0 degrees centre of mass angle for the $L = 0$.

2.2 Wavelet analysis

Wavelet analysis is an extension of Fourier analysis which allows for the conservation of the correlation between the observables and its transform. Wavelet transforms have advantages over traditional Fourier transforms for representing functions that have discontinuities and sharp peaks. In wavelet analysis, data analysis is performed using scale, and these scales play an important role in the interpretation of data. As an example, one will notice big features if a signal or function is seen through a large window. Similarly small features will be seen for a small window. It is important to note that the wavelet analysis scale (equivalent Fourier scale or wavelength) value is twice the full width at half maximum (FWHM) of the underlying peak in the spectrum.

The wavelet analysis procedure involves the selection of a wavelet prototype, referred to as a Mother-wavelet [Gra95]. The contracted high-frequency version of this Mother-wavelet conducts the time-based analysis and a dilated low frequency version conducts the frequency analysis. The selection of a particular wavelet as the Mother-wavelet depends on the set of predefined mathematical criteria [She05] outlined in the formalism of wavelet analysis.

2.2.1 Formalism of wavelet analysis

A real or complex function $\Psi(x)$ can only be used as a Mother-wavelet if:

$$\int_{-\infty}^{\infty} \Psi^*(x)dx = 0, \tag{2.25}$$

and

$$K_\Psi = \int_{-\infty}^{\infty} |\Psi^2(x)| dx < \infty, \tag{2.26}$$

where $\Psi^*(x)$ is the complex conjugate of $\Psi(x)$ and K_Ψ is the wavelet norm.

The first condition satisfies the requirement of an oscillating function for which the mean value must be zero in the absence of an imaginary component [She05]. The restriction of the function to a finite domain is required in the second condition. Wavelets are localised both in time and in frequency, so they are unaffected by the properties of the data far away from the region of interest and as such, are ideal for the description of the local behaviour [Don16].

Wavelet analysis is performed using two types of wavelet transform, namely Continuous Wavelet Transform (CWT) and Discrete Wavelet Transform (DWT). Both techniques can be used to represent a continuous excitation energy spectrum. The continuous wavelet transform is applied in the present study.

2.2.2 Continuous Wavelet Transform

The coefficients of the wavelet transform of some data sample or spectrum $\sigma(E)$, following its convolution with the wavelet function are given by

$$C(\delta E, E_{\mathrm{x}}) = \frac{1}{\sqrt{\delta E}} \int \sigma(E) \Psi^* \left(\frac{E_{\mathrm{x}} - E}{\delta E} \right) dE, \tag{2.27}$$

where δE is the bin size and its purpose is to scale the function. E_{x} is responsible for shifting the position of the wavelet in excitation energy and, therefore, provides access to the scale localisation information.

The original spectrum can be reconstructed from the wavelet coefficients through the use of the inverse wavelet transform:

$$\sigma(E) = \frac{1}{K_\Psi} \int_{-\infty}^{\infty} \int_{0}^{\infty} C(\delta E, E_{\mathrm{x}}) \frac{1}{(\delta E)^{\frac{5}{2}}} \Psi \frac{E_{\mathrm{x}-E}}{\delta E} dE_{\mathrm{x}}. \tag{2.28}$$

2.2.3 Wavelet-based semblance analysis

Wavelet-based semblance analysis is a measure of the cross correlation of two datasets. It provides a quantitative measure of the correspondence between the two sets of wavelet coefficients. The wavelet-based semblance S is expressed as

$$S = cos^n(\theta), \tag{2.29}$$

where n is an odd integer greater than zero and it yields values ranging from -1 (inversely correlated) through 0 (uncorrelated) to $+1$ (correlated), θ is the local phase ranging from $-\pi$ to π and is given by:

$$\theta = tan^{-1}[\Im(CWT_{1,2})/\Re(CWT_{1,2})], \tag{2.30}$$

where the cross-coefficient $CWT_{1,2} = CWT_1 CWT_2^*$, CWT_1 is the wavelet transform of data set 1 and CWT_2^* is the complex conjugate of data set 2. $\Re$ and $\Im$ are the real and imaginary parts, respectively.

One method through which two time series can be compared using wavelets is called the cross-wavelet transform [Tor98] and is defined as:

$$CWT_{1,2} = CWT_1 \times CWT_2^*. \tag{2.31}$$

Chapter 3

Experimental method

The experiment for the current project (PR275) was done at iThemba LABS in the Western Cape, by performing measurements of the (p,t) two neutron pick-up reaction on ^{22}Ne using the K600 magnetic spectrometer at zero degrees. A proton beam with an energy of $E_{\mathrm{p}} = 80$ MeV was provided by the Separated Sector Cyclotron (SSC) facility. Figure 3.1 shows the layout of the SSC facility.

The protons were first accelerated in the Solid Pole Injector Cyclotron 2 (SPC2) with an energy of 3.74 MeV, and delivered to the SSC where they were accelerated to the required energy, which is $E_{\mathrm{p}} = 80$ MeV. From there the protons were guided to the K600 magnetic spectrometer vault through the X, P_1, P_2 and S beamlines.

3.1 K600 magnetic spectrometer

The K600 magnetic spectrometer shown in Fig. 3.2 is a facility that is used by scientists world-wide for the study of nuclear structure and reaction mechanisms at intermediate beam energies using light-ion projectiles. Its name is derived from its K-value, which defines the maximum magnetic rigidity of charged particles for which it is designed. The K-value is calculated as:

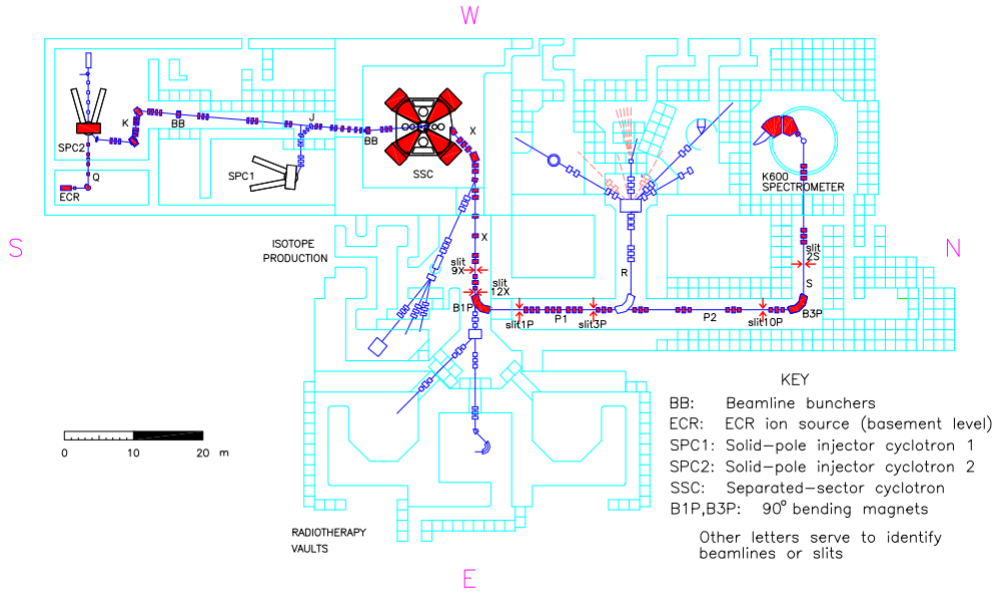

Figure 3.1: The iThemba LABS Separated Sector Cyclotron (SSC) facility.

$$K = \frac{mE}{q^2}, \tag{3.1}$$

where m is the atomic mass number of the particle, q is the charge, and E is the kinetic energy in MeV [Weg87].

The design of the K600 spectrometer of the Indiana University Cyclotron Facility (IUCF) has led to the development of the K600 magnetic spectrometer at iThemba LABS. Late in the 1990's, the K600 from IUCF was decommissioned, and is now part of the beamline leading to the Grand Raiden magnetic spectrometer [Fuj99] at the Research Center for Nuclear Physics (RCNP) in Osaka, Japan. The Grand Raiden magnetic spectrometer can achieve high energy-resolution measurements at $\theta_{\text{lab}} = 0°$ with medium energy proton beams in the range of $E_{\text{beam}} = 50 - 400$ MeV [Nev11].

The K600 magnetic spectrometer consists of five active elements, namely a quadrupole, two dipole magnets (D_1 and D_2) and two trim coils (K and H) [Nev11]. The dipoles are used to achieve momentum dispersion in the scattering plane. Vertical focusing is achieved by the quadrupole. The two trim coils, which are inside the dipoles, are used to achieve the final focusing at the focal plane. The K-coil is a pole face current winding, introducing

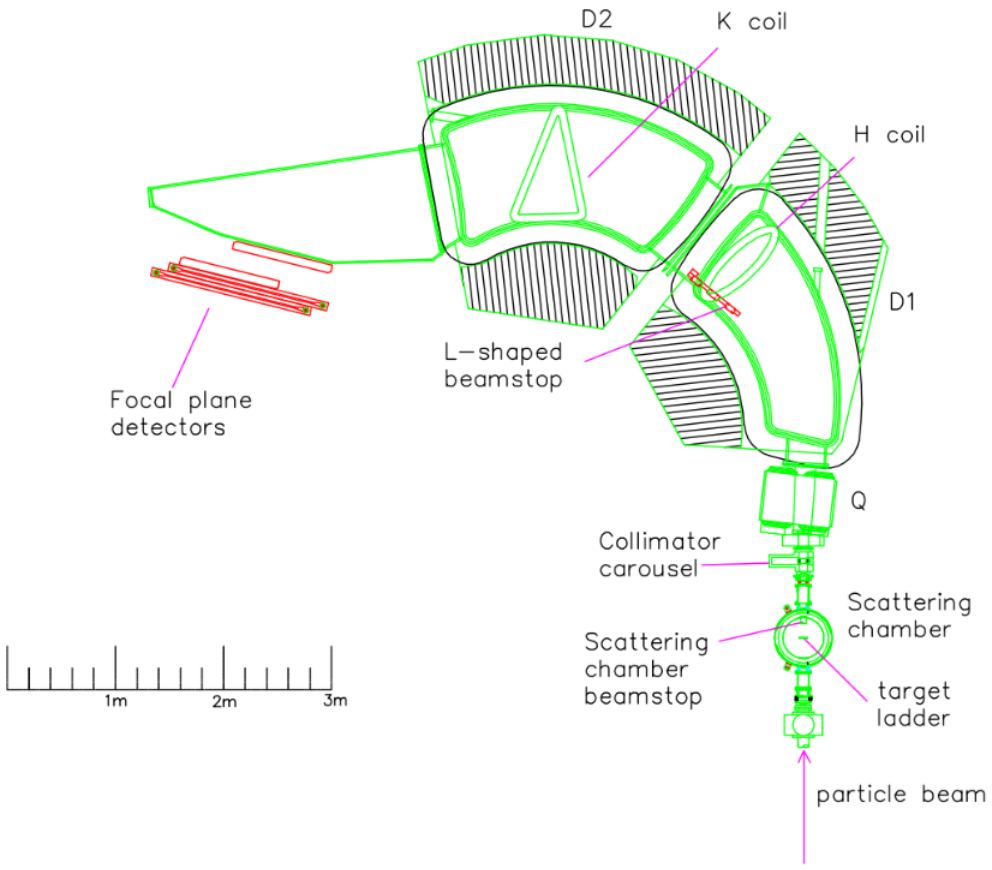

Figure 3.2: The K600 magnetic spectrometer layout for measurements at zero degrees with detectors in the medium dispersion focal plane. The L-shape beamstop was replaced with a smaller beamstop in this experiment (taken with permission from[Nev17]).

both a dipole and quadrupole component, and is used to make adjustments to first-order kinematic variations as a function of scattering angle. The H-coil, which is also a pole face current winding, introduces both a dipole and hexapole component, and is used to correct for second-order abberations.

In the past, the K600 magnetic spectrometer was used successfully to study the (p,t) reaction at different energies with good energy resolution. In studies of this reaction the K600 can be operated in the zero degree mode or at a range of larger scattering angles. Triton excitation-energy spectra with a typical resolution of 40 keV (FWHM) at $E_{\mathrm{p}} = 60$ MeV [Swa15], 32 keV at $E_{\mathrm{p}} = 100$ MeV and 48 keV at $E_{\mathrm{p}} = 200$ MeV have been measured [Nev11]. Such high energy-resolution (p,t) spectra can be obtained without significant particle background contaminants. It is, therefore, an ideal experimental tool for investigating excited states in ^{20}Ne by using the (p,t) reaction on a ^{22}Ne gas target at $E_{\mathrm{p}} = 80$ MeV.

3.2 K600 focal plane detector package

The focal plane detector system used in a typical K600 measurement consists of Vertical Drift Chambers (VDCs) and plastic scintillators situated behind the VDCs. The position information along the length of the focal plane as well as the angle at which a charged particle crossed the focal plane is determined using the VDCs. The scintillators provide the event trigger for the VDCs to start collecting drift time information. In the present experiment, only one VDC and two plastic scintillators were in the focal plane setup during the data collection period, as shown in Fig. 3.3. Only one scintillator yielded a signal from the tritons since the tritons lost most of their energy in the first scintillator and, therefore, could not reach a second scintillator.

3.2.1 Vertical drift chambers

The vertical drift chambers used at iThemba LABS are also known as Multi-Wire Drift Chambers (MWDC). When charged particles move through the detector they cause the ionisation of gas molecules. The free electrons

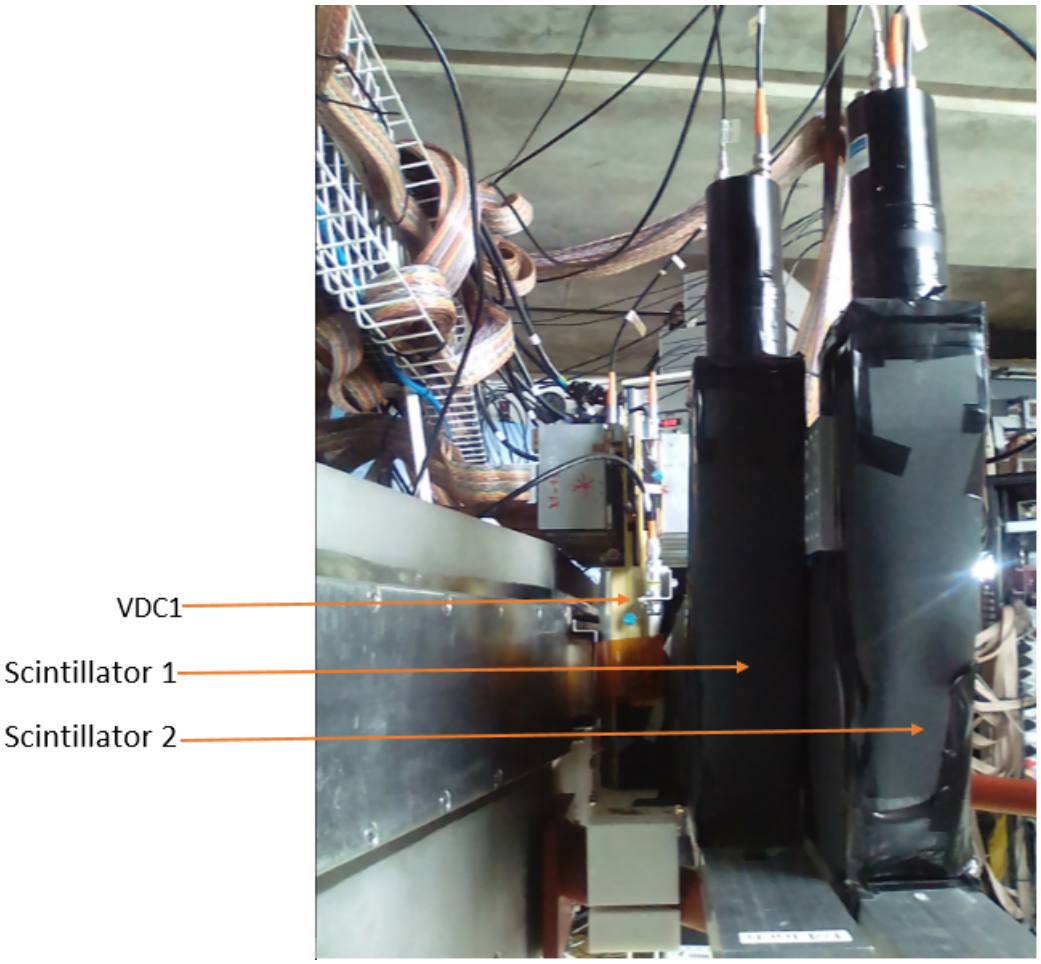

Figure 3.3: The focal plane detector package employed during the data collection period for the present experiment. The charged particles exit the K600 vacuum chamber and move through the detectors from left to right. The first detector on the left is the VDC1, followed by the first and second scintillators to the right of it.

drift towards signal wires under a uniform electric field, where electron avalanching takes place to induce an electric signal [Ber77]. The arrival times of the pulses at the different wires are recorded. Hence, the position where an incident particle crosses the focal plane may be determined if the drift velocity of electrons within the chamber is known [Ber77]. This is important in order to have the position sensitivity which will result in the necessary excitation energy resolution through track reconstruction.

During the experiment only one VDC, referred to as an X-U VDC, was used. This VDC consists of an X wire plane with 201 guard wires and 198 signal wires, all placed vertically, as well as a U wire plane with 146 guard wires and 143 signal wires which are slanted at 50 degrees with respect to the horizontal plane. The U plane makes it possible to acquire vertical position information in addition to the horizontal focal plane information from the X wire plane.

The guard wires consist of 50 μm diameter gold-plated tungsten wires and the signal wires are made of 20 μm diameter gold-plated tungsten wires, interspersed between the guard wires [Nev11]. The thinner signal wires are used to record the data, whereas the thicker guard wires are put at approximately -500 V and define drift cells to individual signal wires, with widths of $\sim$1.7 mm and extending 8 mm on both sides of the wire plane to the HV planes. The HV planes are made of aluminium foils, and a negative high voltage of 3600 V was applied to them.

3.2.2 Scintillator detectors

The scintillators are made of BC-408 plastic scintillator material [Cry18], wrapped in aluminised mylar to make them light tight. They are 122 cm wide, 10.2 cm tall and either 1.22 cm or 0.635 cm deep. These scintillators are connected by adiabatic light guides to photomultiplier tubes at both ends, from which the signals go to the electronics [Nev11]. The scintillators and their photomultiplier tubes are covered by a thin layer of paper to shield the photomultiplier tubes and light guides from light within the vault. The trigger signals for data collection are provided by the coincidence signals from both sides of a plastic scintillator. The signals from the scintillators also provide energy loss and Time-Of-Flight (TOF) information which can be

used to generate Particle IDentification (PID) spectra.

The time differences between scintillator trigger signals and the beam Radio Frequency (RF) signal are used to generate TOF information. The TOF ranges of different particles were determined from their energy ranges. From the known energy range of tritons that will be investigated, between $46 - 56$ MeV, the corresponding rigidity range $1713 - 1883$ kG.cm that the K600 will accept was determined. The momentum P (in MeV/c) for all other particles that can reach the focal plane was determined from the known rigidity values:

$$P = c \times QB\rho \times q, \tag{3.2}$$

where c is the speed of light, $QB\rho$ is the rigidity and q is the charge of the particle.

Hence, from momentum P, kinetic energy ranges E of the different contaminent particles are determined using

$$E = \sqrt{P^2 + m^2} - m, \tag{3.3}$$

where m is the mass of the particle in MeV/c^2.

In order to determine which particles will reach the focal plane, approximate values of the range of absolute TOF values associated with different particles (tritons, deuterons and protons) for the different energy ranges are calculated using

$$TOF = \frac{d}{v}, \tag{3.4}$$

where d is the distance covered by the particle and v is its velocity, calculated as:

$$v = c \times \sqrt{1 - \left(\frac{M}{E_T}\right)^2}, \tag{3.5}$$

where c is the speed of light, M is mass of the particle, and E_T is the total energy. The distance d varies between the minimum and maximum flight path values in the K600 of $d = 7.78$ m and $d = 8.87$ m for a particle traveling from the target to the medium dispersion focal plane. Table 3.1 shows the TOF ranges for the triton magnet setting for the K600 for the particles mentioned above.

Table 3.1: The TOF ranges of tritons, deuterons and protons at triton energy setting.

Particles	Triton energy range (MeV)	TOF-range (ns)
tritons	46 - 56	145 - 150
deuterons	69 - 83	98 - 103
protons	131 - 157	54 - 57

Table 3.1 shows that the tritons and deuterons should be separable in time. Protons will not be seen on the focal plane due to energy cosiderations. In order for them to fall within the rigidity range where they could be seen in the focal plane if the spectrometer's magnets are set for 46-56 MeV tritons, these protons will need to have kinetic energies far above that of the beam energy ($E_{\mathrm{p}} = 80$ MeV).

3.3 Gas target system

The gas target system used during the experiment consisted of two gas cells which were placed in the top two positions of the target ladder. The gas cell consists of a combination of a body of aluminium with a plastic foil on either side, clamped onto the body by two aluminium end plates. A drawing of the 10 mm thick body of the gas cell is shown in Fig. 3.4. The gas cell windows are aramid foils with a thickness of 5.5 μm. The full target ladder is shown in



Figure 3.4: A drawing of 10 mm thick gas target cell.

Fig. 3.5. The gas handling system was placed outside the scattering chamber, and a schematic of the system is shown in Fig. 3.6.

3.3.1 Gas handling system

The target pressure needed in the present experiment was approximately $P =$ 1.3 bar. This pressure was needed so that a target thickness in the region of 1.6 mg/cm^2 could be achieved for the 10 mm thick gas cell. A ^{22}Ne gas bottle provided by Chemgas [Che18] with volume $V = 0.4$ l, and pressure $P = 1.25$ bar was used. The isotopic purity of the ^{22}Ne gas was close to 100%, and the chemical purity of the gas is shown in Table 3.2. The gas control system illustrated in Fig. 3.6 and pictured in Fig. 3.7 was developed in order to preserve gas material while maintaining a sufficiently high and constant pressure in the gas target cell.

The requirement for constant pressure and the relatively low pressure in the Chemgas gas bottle led us to the current method of compressing the gas, shown in Fig. 3.6. A compressor was used in order to increase the gas pressure. The pressure of the gas in the target cell was subsequently controlled by a pressure regulator and a flow rate meter, both made by Bronkhorst [Bro18]. It was important to have constant pressure during the experiment, to avoid lower or



Figure 3.5: The target ladder with two gas cells at the top.

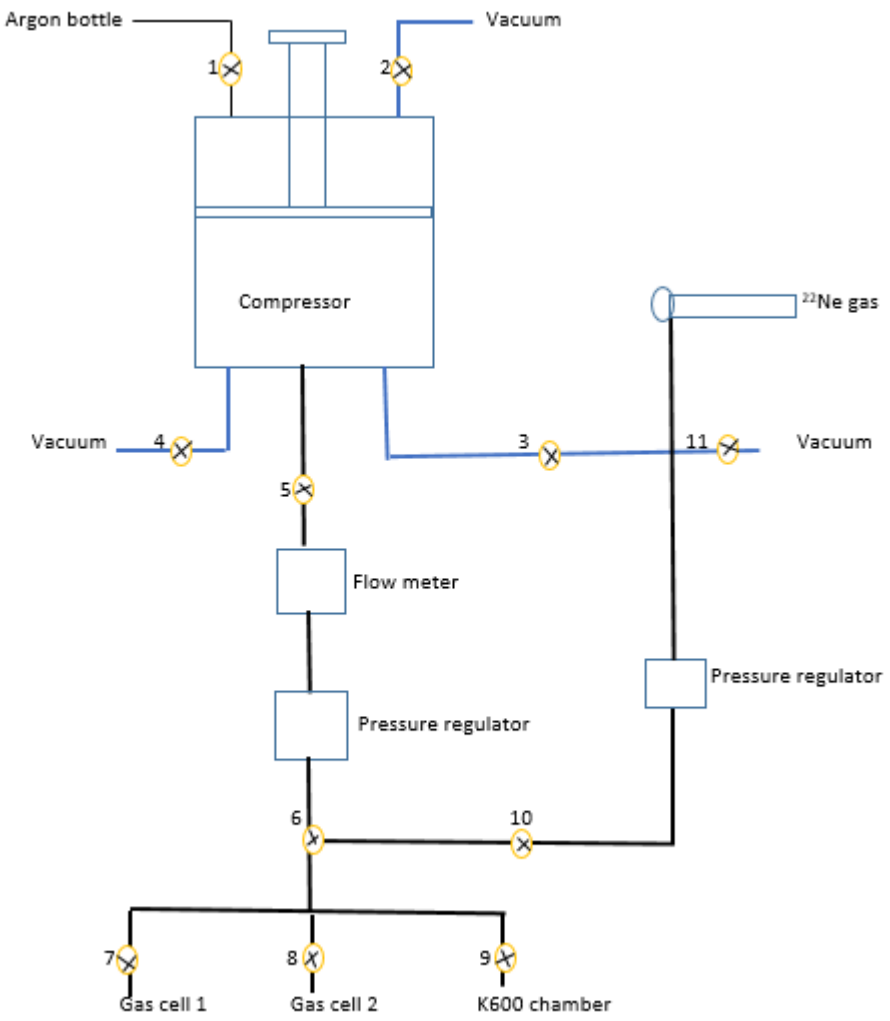

Figure 3.6: A schematic of the target gas cell gas handling system.

Table 3.2: Chemical purity of the ^{22}Ne gas bottle used.

Chemical	Chemical purity
^{22}Ne	99.97 %
^{21}Ne	0.001 %
^{20}Ne	0.03 %
^{3}He+^{4}He	10ppm
N_2+CO	0.015 %
O_2+Ar	5ppm
CO_2	5ppm
H_2	0.015 %
CH_4	5ppm
C_2H_6	2ppm
Others	2ppm

higher gas pressure which results in a thinner or thicker target, which causes lower or higher energy loss, respectively. The pressure was kept constant also to ensure the same energy calibration and energy resolution throughout the experiment.

The Bronkhorst flow meter (model number: F-110C-005-AGD-22-V) and pressure regulator (model number: P-602CV-6K0A-AGD-22-V) were used in the experiment with the purpose of controlling and monitoring the gas cell conditions. A second Bronkhorst pressure regulator (model number: P-602CV-350A-AGD-22-V) was used to protect the gas cell against over-pressure and to leak high pressure gas to the region between valves 3 and 11 in Fig. 3.6, since it was observed that the gas pressure at the gas cell was increasing outside of the gas-filling times. The various connections of this system were made of polyethylene pipes with a diameter of 1/8th inch. Steel valves were used to control the gas flow, and to evacuate the gas by using a vacuum pump. The gas handling system was developed to ensure proper delivery and control of the gas to the gas cell.

Figure 3.7 shows a photograph of the gas handling system setup used during the experiment. Firstly, before filling all the piping with highly enriched ^{22}Ne gas, one must ensure that there is nothing else in the piping or the target cell, in order to avoid contamination to the gas cell with air. Only after the pipes were evacuated with a vacuum pump the ^{22}Ne gas was then allowed through

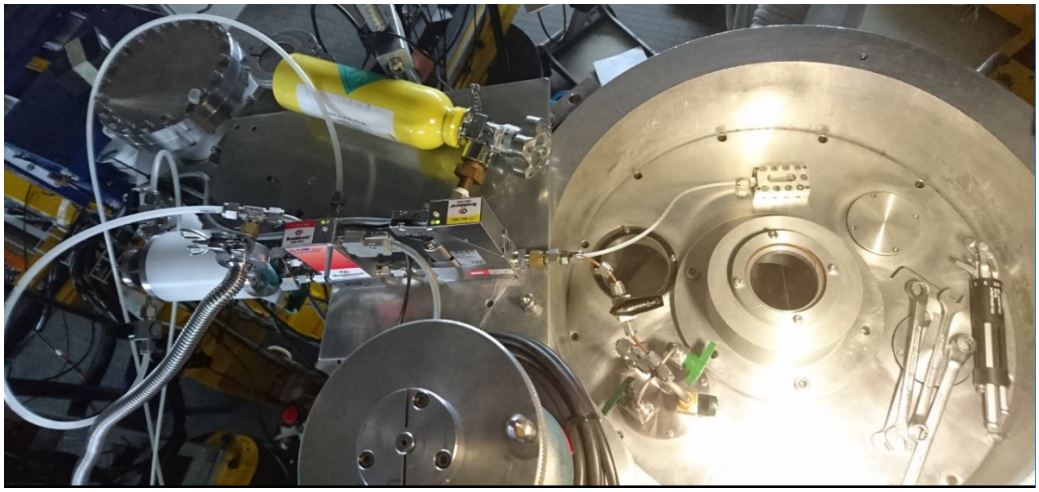

Figure 3.7: The target gas cell gas handling system.

the gas pipes into the gas cell. The gas was first allowed into the compressor, before reaching the gas cell. The plunger was moved down using high pressure gas supplied by an argon gas bottle, and gas delivered to first gas cell was controlled using the pressure regulator and flow meter. Gas cell 2 was used as a back-up, in case gas cell 1 broke.

Figure 3.8 represents an example of the gas pressure and flow rate with respect to time. The flow rate peaks correspond with a small decrease in the pressure, when the pressure controller allowed gas through to make up for the slight loss of pressure. This clearly ensured very small pressure changes throughout the experiment. The maintenance of nearly constant pressure over a period of six hours is illustrated by how the red spectrum remains approximately flat.

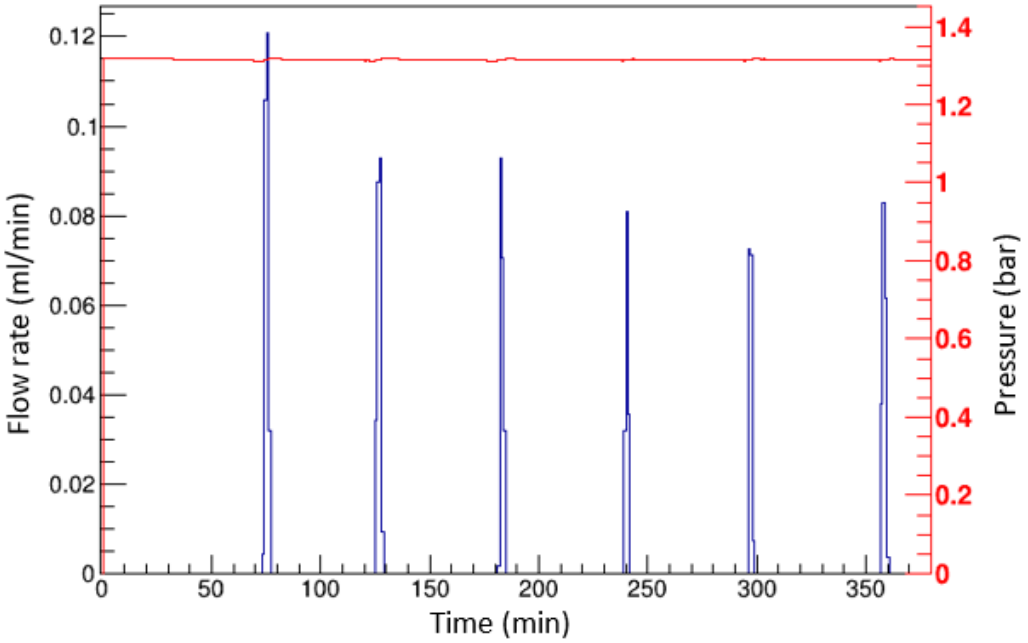

Figure 3.8: Graph showing gas pressure and flow rate with respect to time.

3.4 Electronics and DAQ

Electronic modules adhering to the Nuclear Instrumentation Module (NIM) and Versa Modula Europe (VME) standards were used to convert the electrical signals from the focal plane detectors into digital information that could be processed by the Maximum Integration Data Acquisition System (MIDAS) software [Ins18].

3.4.1 Trigger logic

Figure 3.9 represents a block diagram of the trigger logic electronics in the spectrometer vault. Two Photo-Multiplier Tubes (PMTs) were used to provide the signals for the trigger electronics. The PMTs were attached to light-guides on opposing sides of a scintillator. The signal provided by each PMT was sent to a Linear Fan (Lin Fan) which makes a copy of the input signal and provides an output to the Charge-to-Digital Converter (QDC) to be digitised, as well as to the Constant Fraction Discriminator (CFD). The CFD converts the linear signal to a logical signal, where the timing of the output signal is

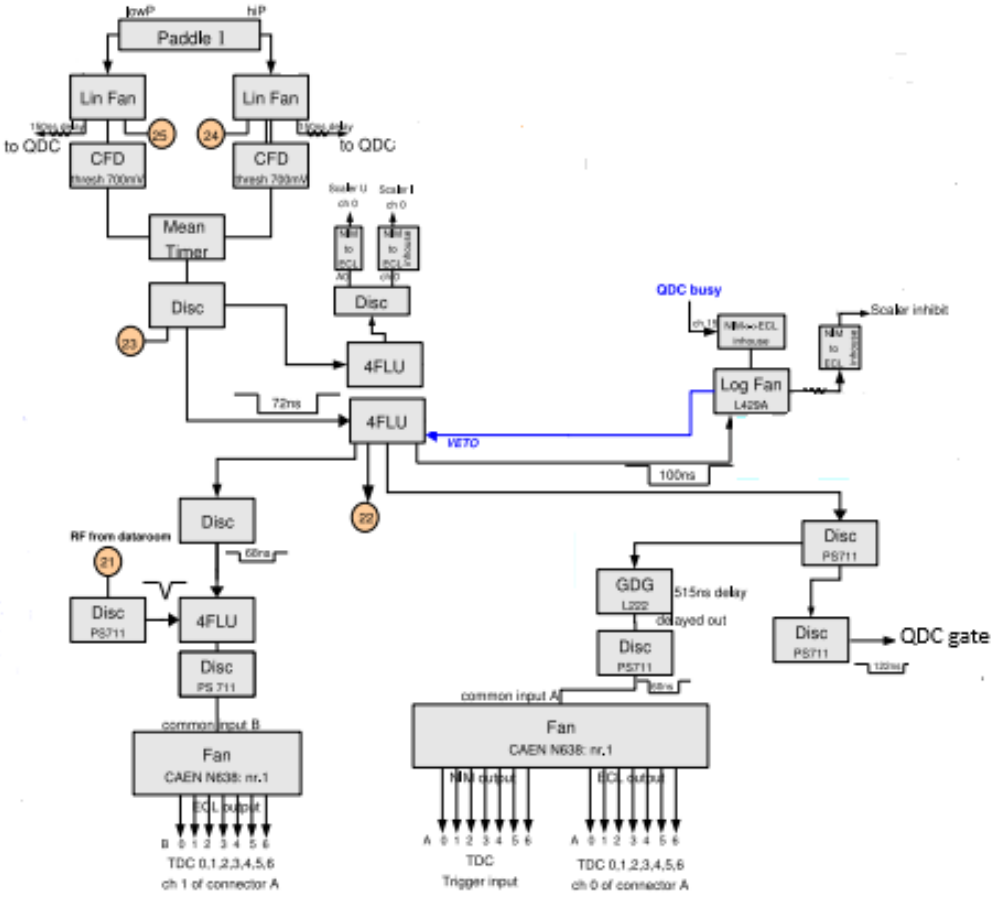

Figure 3.9: The trigger electronics diagram.

independent of the amplitude of the input signal. The output from both CFDs were sent to the mean timer which makes the timing of the output from the mean timer independent of the position where the ejectile particle traversed the scintillator. The output from the mean timer is shaped by a discriminator, and then sent to a four-Fold Logical Unit (4FLU) which operates in an OR mode since only one scintillator was used.

The output signal from the OR logical unit is sent to the QDC gate input which triggers the DAQ. Seven copies of the signal are made and each is sent to an individual Time Digital Converter (TDC) which records the time, after being shaped by the discriminator. Another signal from the OR logical unit is shaped by the discriminator to be used together with the RF signal from the SSC in an AND logical operation to produce a TOF signal. Multiple copies of this TOF signal are made and sent to individual TDCs.

3.4.2 Pre-amplifier cards and TDCs

The signal wires of the VDCs are connected to Technoland PTM 005 16-channel pre-amplifier cards via signal wire tracks on the printed circuit board of the wire plane of the VDC. The pre-amplifier cards amplify the signals from the signal wires, and perform a discriminatory function to ensure that only proper signals go through to the time-to-digital converters (TDCs). The 16-channel twisted pair ribbon cables form the connection between the pre-amps and the TDCs. In total, 13 pre-amplifier cards are used for the 198 signal wires in the X-wire plane, and for the 143 signal wires in the U-wire plane, 9 pre-amplifiers are required [Nev17]. The X-plane pre-amplifier cards are situated on the same side as the signal wire tracks, whereas the U-plane pre-amplifier cards are situated on the opposite side of the signal wire tracks.

3.4.3 Current integration

In order to measure beam current the beam stop inside the K600 was connected to the Brookhaven Instruments Corporation Model 1000C Current Integrator (CI) in the data room. The CI generates output pulses at a frequency of 1 kHz at full-scale current setting. For example, for a beam current of 1 nA the CI will yield an output of 500 Hz if the CI scale is set to 2 nA. The digital output from the CI was sent through shaping electronics to the input of a VME scaler module CAEN V830. Calculation of the integrated current is done using the scaler in conjunction with the known CI full-range setting [Nev17].

3.4.4 Data acquisition

As indicated earlier, digitisation of the electronic signals was done using VME hardware. Three types of VME modules namely a VME QDC (CAEN V792), VME scalers (CAEN V830), and VME TDCs (CAEN V1190) were used.

The data acquisition package written in C++ and known as MIDAS was used to process and assemble the digital information from the VME modules. The MIDAS software package consists of libraries which can be used for data

transport and a set of programs for data logging and system management [Ins18]. A fast online database, in which the experimental configuration is stored, and a web interface, which makes the experiment remotely controllable, are additional features of MIDAS.

3.4.5 System dead time measurement

The system dead time is measured with a pulser and two scaler modules, namely the inhibited and uninhibited scalers. The uninhibited count is generated by sending the pulser signal to one scaler module. The same pulser signal is also counted by the other scaler, which is vetoed by the system busy signal from the QDC to create the inhibited count. The system dead time could be determined by comparing the number of pulses measured by the two scaler modules.

3.5 Experimental procedure

The magnetic spectrometer and its electronics described in the previous sections were set up before the experimental period. The beamstop was placed between the dipole magnets of the K600 (D1 and D2) as shown in Fig. 3.10. The scattering chamber was pumped down to $P = 5 \times 10^{-5}$ mbar with the target ladder in the chamber. The magnets were switched on and set to the appropriate field (D1 = 343.58 T) to measure tritons in the spectrometer focal plane using the ^{22}Ne(p,t) reaction at zero degrees. This allows for the measurement of excitation energies in ^{20}Ne in the region on 15 - 25 MeV. The magnetic fields were set by adjusting the beam currents in the electromagnets via remote control from the data room.

Finally, the data were collected with the trigger rate using different targets, ranging between 250 Hz to 1500 Hz, and the beam current ranging between 4 nA to 5.5 nA. The data were collected at $\theta_{\mathrm{lab}} = 0^{\circ}$ with a beam energy of $E_{\mathrm{p}} = 80.6$ MeV. The Q-value of the ^{22}Ne(p,t)^{20}Ne reaction is $Q = -8.64$ MeV, so with a 80.6 MeV beam one could expect to measure the candidate 5-alpha cluster state of ^{20}Ne at a triton energy of $E_{\mathrm{t}} = 49.005$ MeV. The ^{22}Ne

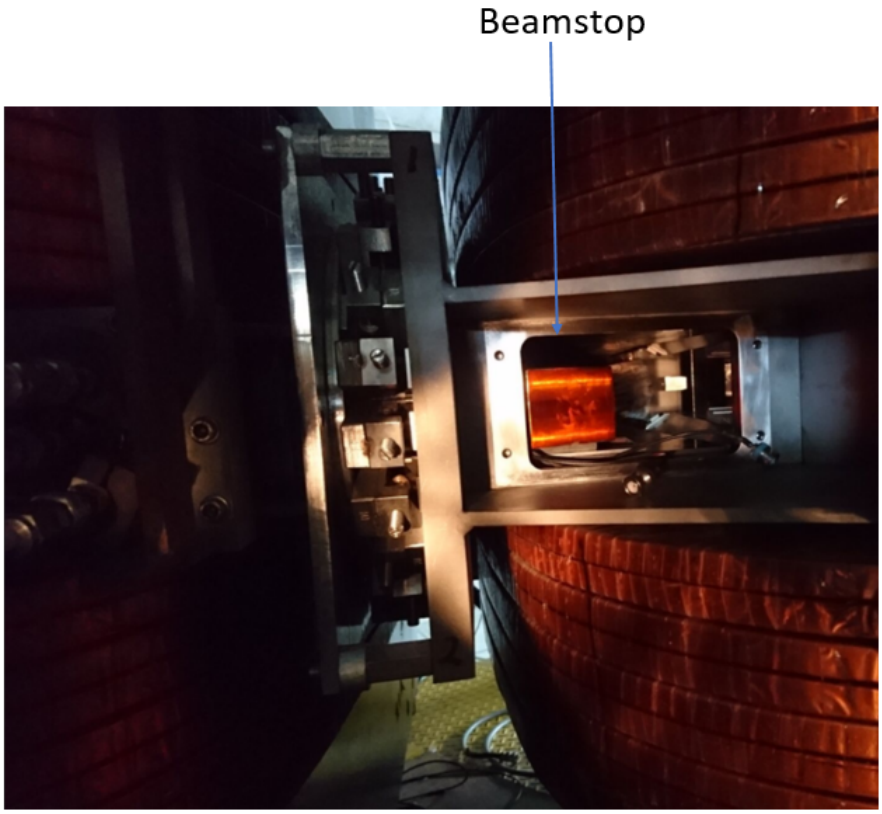

Figure 3.10: The zero degree beamstop placed between dipole magnets.

gas was put into the target cell at a pressure of $P = 1.3$ bar. Gas pressure was monitored with a pressure regulator. The ^{22}Ne data collected is represented by 9 runs, and the time of each run varied between 30 minutes and one hour. Data were also acquired for aramid foils, with the purpose of identifying tritons originating from aramid in order to differentiate them from tritons originating from Ne. The total number of aramid runs collected were 6. The duration for each run was 30 minutes. In between the ^{22}Ne and aramid data, the data were collected regularly for an empty target in order to identify background from beam halo.

Chapter 4

Data analysis, results and discussion

A C++ user code which translates the raw MIDAS [MID19] files into ROOT [ROO19] files was developed at iThemba LABS. The code functions within the MIDAS framework. It takes the stored event-by-event data from the scintillators and the VDCs, and sorts it in such a way that the detector's responses for each event can be known. This can then be used in an online and offline data analysis. An event is the result of a nuclear reaction detected by the focal plane detectors.

The code was written specifically for the focal plane detector package of the K600 magnetic spectrometer. The important pieces of the code for the analysis of the present experiment includes qdc.c, scaler.c, beamline.c, Focalplane.c and main.c. The file qdc.c is responsible for extracting the QDC information from the raw midas files, whereas scaler.c extracts the scaler information from the raw midas files. The code beamline.c collects the EPICS variables from the local network, for example information about the pressure and flow rate of the gas target system, which is discussed in the experimental method chapter. The extraction of the TDC information to calculate all parameters relevant for the focal plane detectors is the purpose of Focalplane.c and main.c.

The code main.c populates histogram and TTree data structures for ROOT. Subroutines are defined for associating a wire number with each TDC channel number from the raw data, and calculating the horizontal and vertical positions

of particles at the focal plane and tracing the exact path of particles through the wire plane. All the ROOT histograms and tree structures are defined for the variables that are most important for the data analysis, e.g TOF, paddle light output, wire-plane position, efficiency, etc.

4.1 Particle identification (PID) method

Identification of particles observed in the focal plane detectors may be achieved by obtaining energy loss and time-of-flight information with the scintillator detectors. Different types of particles lose different amounts of energy in a medium. The rate of energy loss of a charged particle with respect to distance travelled through a material is inversely proportional to the square of the velocity (v) and proportional to the square of the charge (Ze), according to the Bethe-Bloch equation [Kno00]:

$$\frac{dE}{dx} \propto \frac{(Ze)^2}{v^2}. \tag{4.1}$$

Each reaction product that leaves the target with its own characteristic mass and energy has its own characteristic velocity. This implies a unique TOF range for each type of particle travelling through the same flight path. Thus, for a given magnetic field, minimum and maximum possible TOFs may be assigned to any particle for which the velocity may be deduced from its known mass and energy. The minimum and maximum estimated flight paths for a particle from the target to the focal plane is 7.78 m and 8.87 m, respectively [Swa10].

Particles with different charge and velocity combinations will, therefore, appear at different locations in an energy-loss versus TOF plot. The PID plot of the energy deposited in the scintillator versus the TOF is shown in Fig. 4.1. A gate was created around the particles of interest, which are tritons. Each locus can be selected and investigated by setting a PID gate around the relevant region. Figures 4.2 and 4.3 are the position spectra with no PID gate and with a PID gate, respectively.

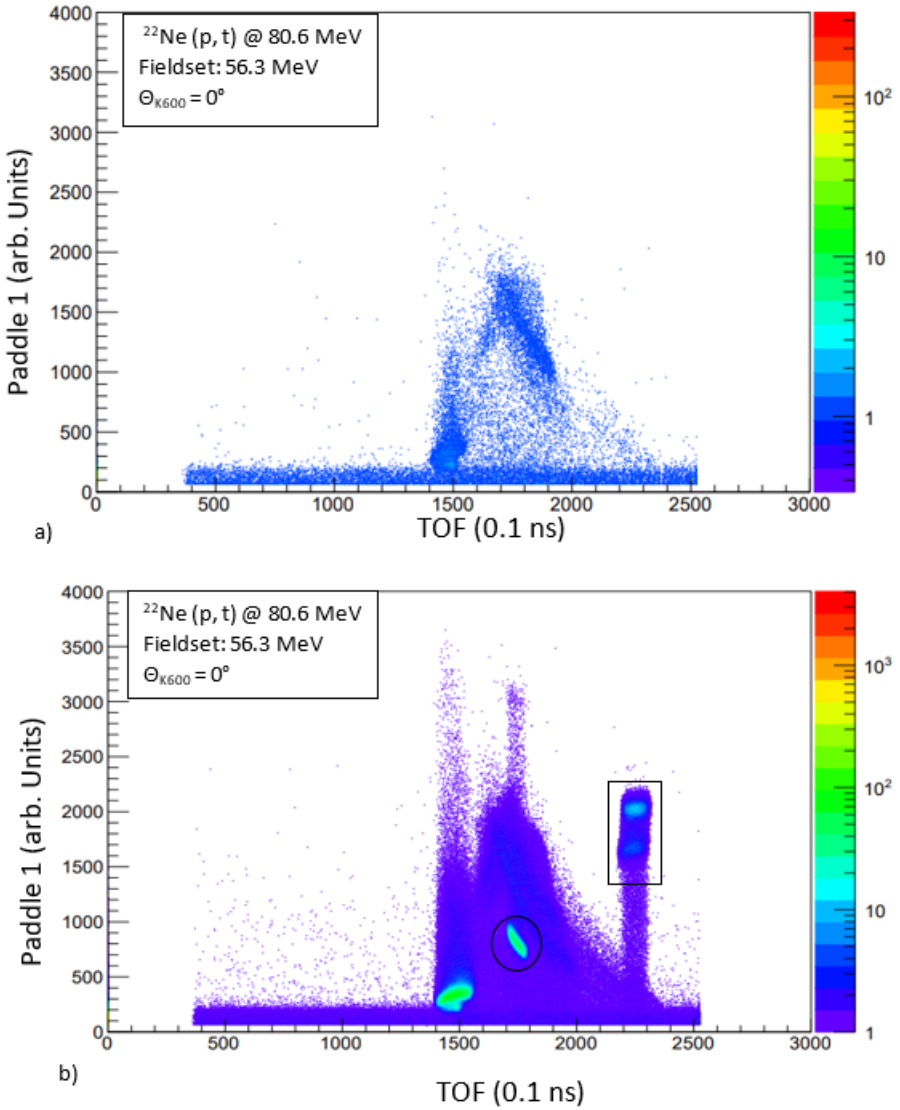

Figure 4.1: (a): A scatterplot of the energy deposited in the scintillator versus TOF for the empty target. (b): A scatterplot of the energy deposited in the scintillator versus TOF for the ^{22}Ne(p,t)^{20}Ne reaction with a 56.3 MeV (p,t) field setting. The black rectangle indicates tritons (particle of interest), the black circle indicates deuterons. The rest represent beam-related background as shown in the top plot.

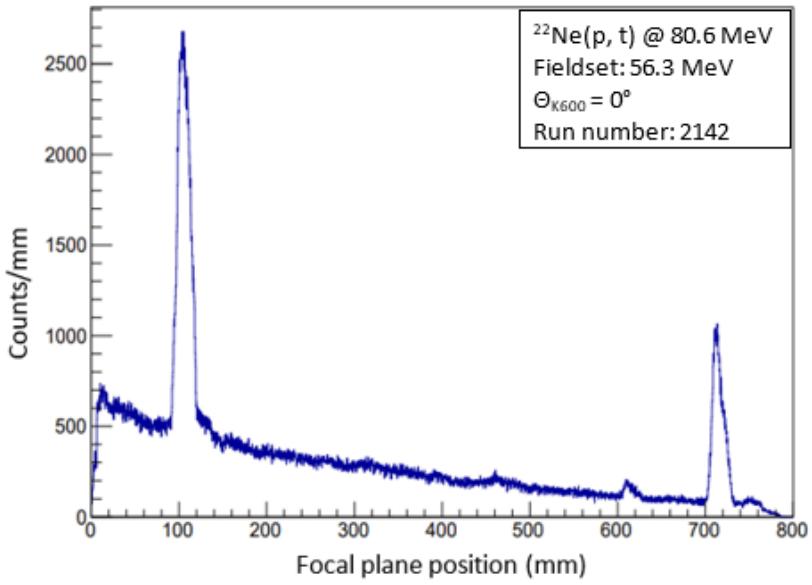

Figure 4.2: Measured position spectrum for the ^{22}Ne(p,t) reaction, without a PID gate as shown in Fig. 4.1. The peak on the left is deuterons whereas the peak on the right is tritons.

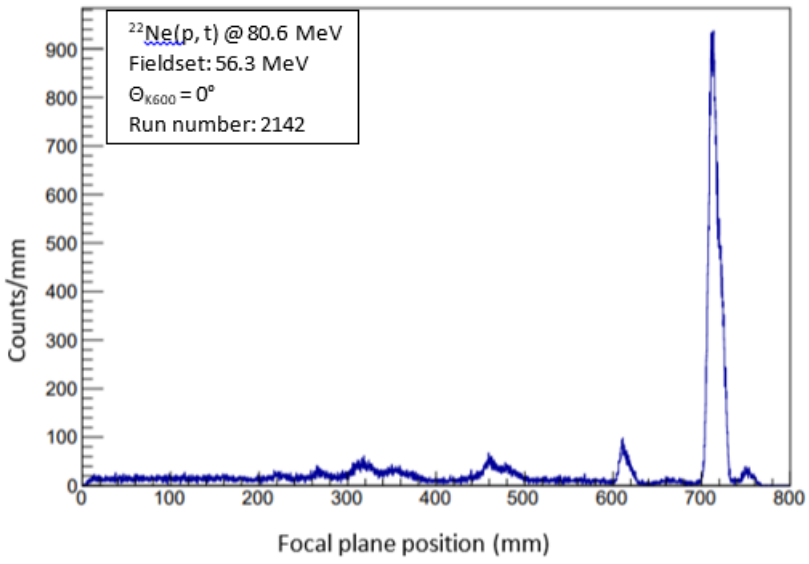

Figure 4.3: Measured position spectrum for the ^{22}Ne(p,t) reaction with a PID gate as shown in Fig. 4.1.

4.2 VDC operation

High voltage is applied to the HV planes in order to provide an electric field that causes the electrons to drift towards the anode signal-wire plane. The electric field does not change, except for the regions very near to the signal wires [Swa10]. A linear time-to-position relationship occurs from the constant electric field over the drift region.

The drift times shown in Fig. 4.4 together with the wire position information for the events are used to determine the focal-plane coordinates for all valid VDC events. The drift times, which are measured from the point of primary ionisation to the point where avalanching occurs in each cell, and the known average drift velocity, yield the LookUp Table (LUT) shown in Fig. 4.5 which is used to determine the drift distance. Figure 4.6 shows the calculated drift distance, and it is calculated for each wire in an event. Hence, the distance from the signal wire to the position where the particle first passes through the drift cell is determined.

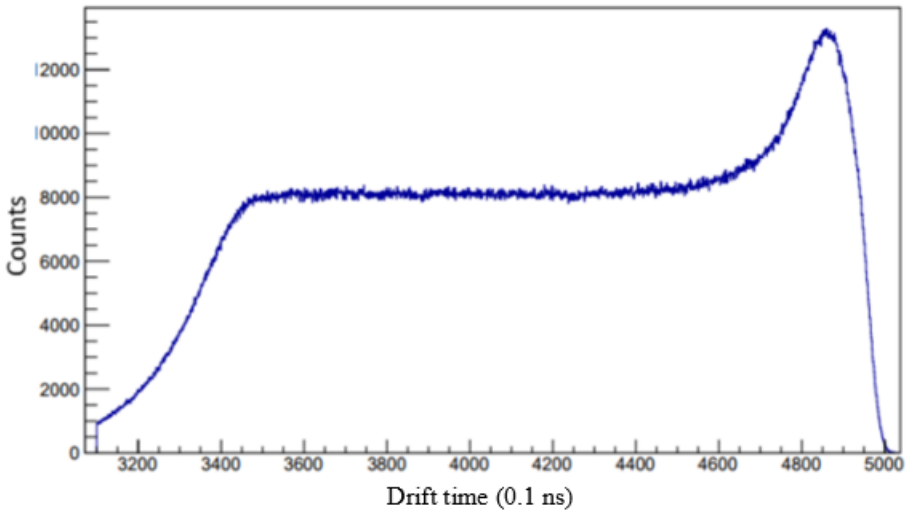

Figure 4.4: The drift time spectrum for the tritons measured in the X-wire chamber.

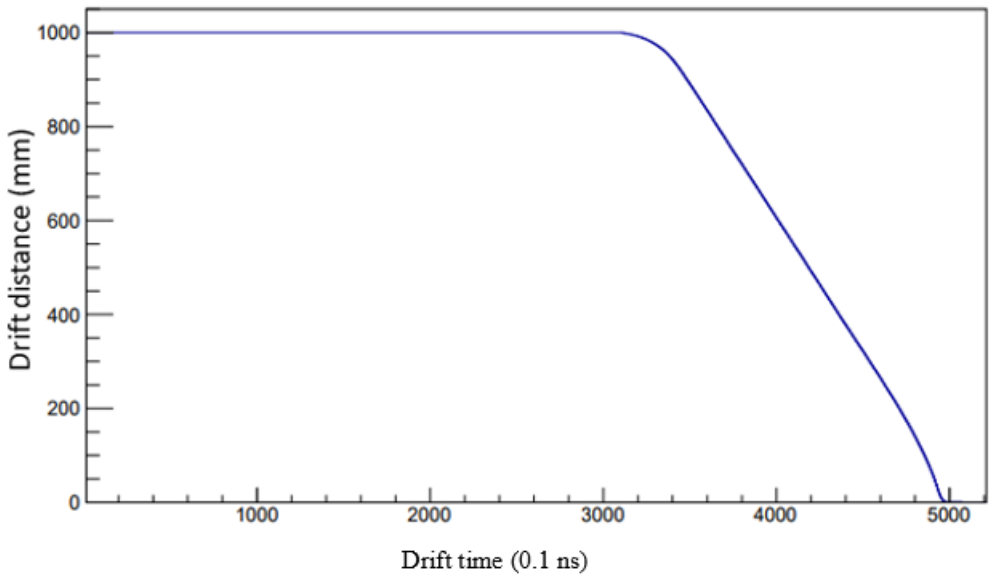

Figure 4.5: The lookup table.

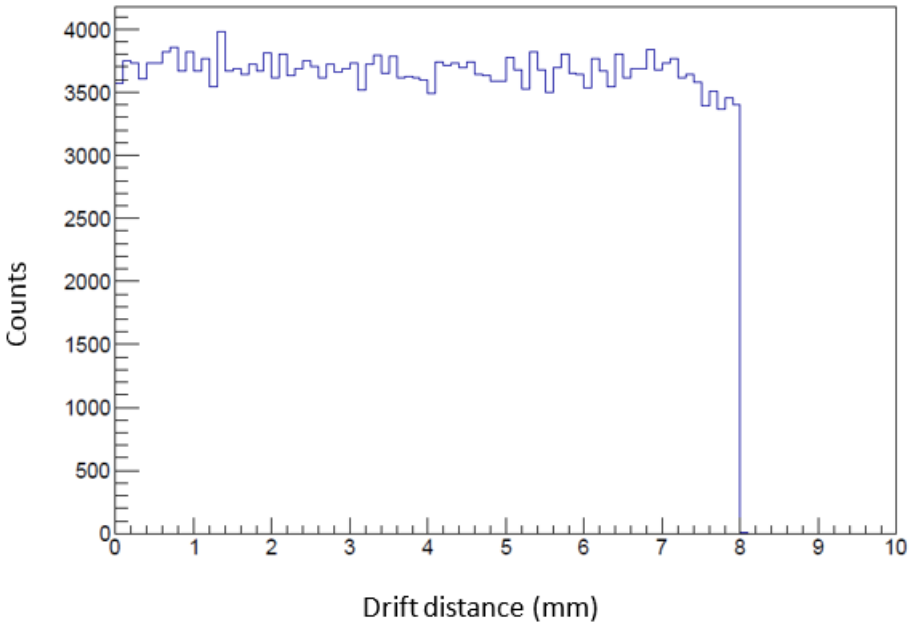

Figure 4.6: The drift distance spectrum corresponding to the drift time spectrum in Fig. 4.4.

4.3 VDC efficiency

The ratio between good events and all selected particle identification (PID) events recorded by a wire chamber gives the efficiency of data collection of a wire chamber. The product of the efficiency of the two wire planes provides the overall detection efficiency ϵ, calculated as

$$\epsilon = \frac{X1_{\text{good}}}{X1_{\text{all}}} \times \frac{U1_{\text{good}}}{U1_{\text{all}}}. \tag{4.2}$$

An event is said to be good if the time-of-flight and scintillator signals are in a good region, and if it includes a minimum of three and maximum of eight consecutive signal wires that registered a hit. The statistical parameter "total sum of squares" of an event must be equal to one or very close to one. Figure 4.7 shows the typical signal wire hit spectrum. During the experiment, efficiencies of 97 to 99 percent were typically measured.

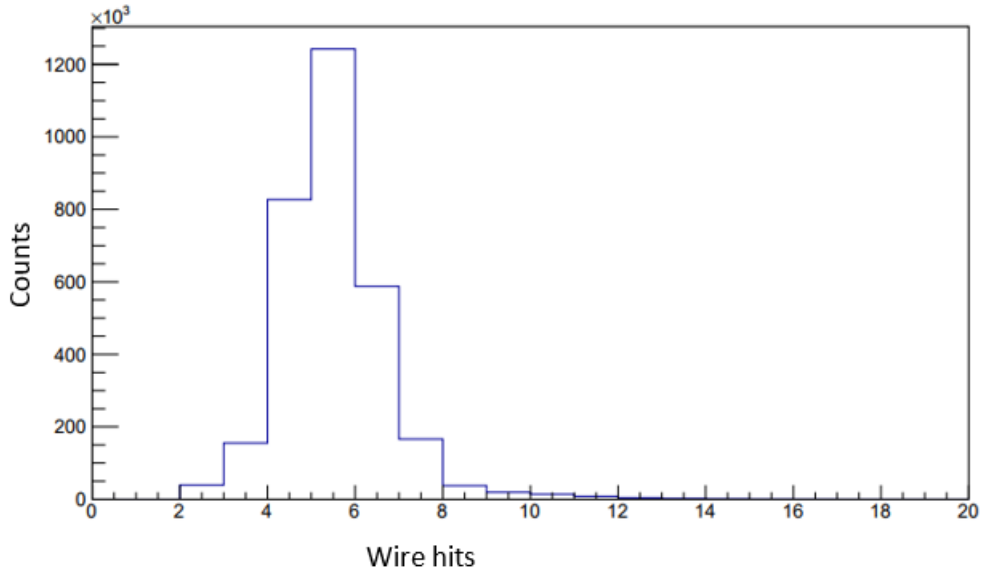

Figure 4.7: The number of signal wire hits per event for VDC X1.

4.4 TOF offsets

During data collection, small variations in TOF occurred, and these variations make it difficult to define software gate settings for the whole experiment. This is solved by determining the TOF offsets, which are important for stabilising the TOF position for the data, and making sure that the TOF peak is in the same spot for all the runs analysed. This must be done since the TOF peaks change position every time the beam intensity is optimised with the SSC radio frequency changes.

The TOF offsets were determined by locating the triton peaks as shown in Fig. 4.8. While the Gaussian peak is not ideally suited for fitting the triton peak in the TOF spectrum, it allows for an adequate determination of TOF shifts between runs. The resulting offset corrected TOF parameter will then ensure that the triton locus never shifts outside of the PID gate as defined in Fig. 4.1. TOF variations that occurred on a run-by-run basis were established, and the TOF offsets were determined for each run relative to a reference run, which is run number 2142. The TOF offsets are shown in Table 4.1. The data were then re-analyzed taking these offsets into account, after which the triton TOF peak position was determined again.

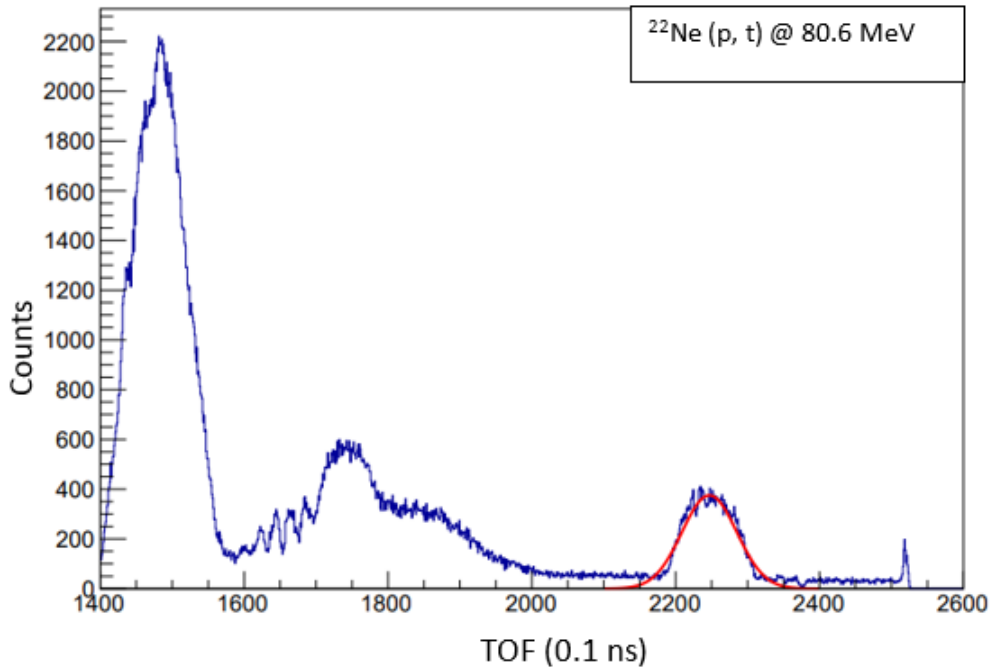

Figure 4.8: A typical TOF spectrum with the peak representing the tritons centered around 225 ns. A Gaussian was fitted to this peak, as shown in red.

Table 4.1: TOF offsets for all the runs with respect to Ne run 2142, the reference run.

Run No.	Clock time	Day	Offsets (ns)
2142	18:31 - 19:36	Sunday	0
2132	12:23 - 12:53	Sunday	6
2137	14:36 - 15:07	Sunday	9
2140	16:24 - 16:31	Sunday	2
2141	16:32 - 16:59	Sunday	15
2143	19:38 - 20:04	Sunday	2
2145	20:09 - 21:09	Sunday	2
2147	21:15 - 22:16	Sunday	1
2148	22:17 - 22:40	Sunday	1
2151	22:58 - 23:56	Sunday	2
2152	23:58 - 00:25	Sunday	2
2154	00:38 - 01:10	Monday	0
2155	01:39 - 02:38	Monday	0
2156	02:40 - 03:41	Monday	0
2157	03:40 - 04:37	Monday	2
2165	05:14 - 06:00	Monday	0

4.5 Lineshape correction

If one plots the focal plane position against the TOF parameter, it is clear that the focal plane position of any particular excited state has a TOF dependence. Line-shape correction is a correction which ensures that the positions of all states are independent of the TOF variable. In this study, it was performed using the TOF instead of the scattering angle since only one VDC was used during the experimental work. Line shape correction was done using run number 2142 (neon run), by plotting TOF vs X1 position, and establishing the line shape correction parameters matching the requirement. The chosen line shape correction parameters are the ones that will optimise the position resolution.

Figures 4.9 and 4.10 represent the TOF vs X1 position spectra for run number 2142 before and after being corrected, respectively. Finally, the corrected position is now assigned to a variable in the ROOT tree. Figures 4.11 and 4.12 represent the position spectrum before and after the correction, respectively.

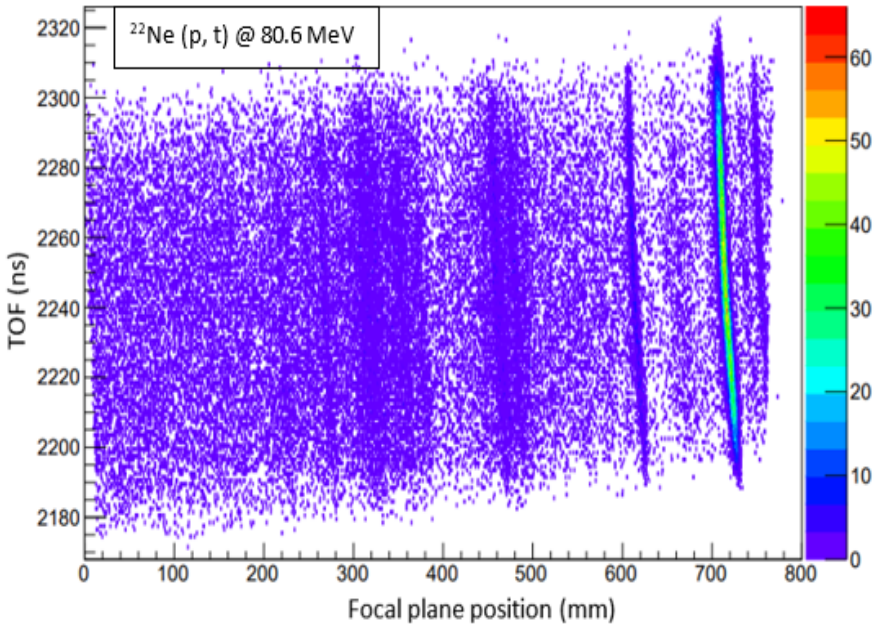

Figure 4.9: A scatterplot of the TOF vs X1 position for the ^{22}Ne(p,t) reaction at zero degrees, without line shape correction.

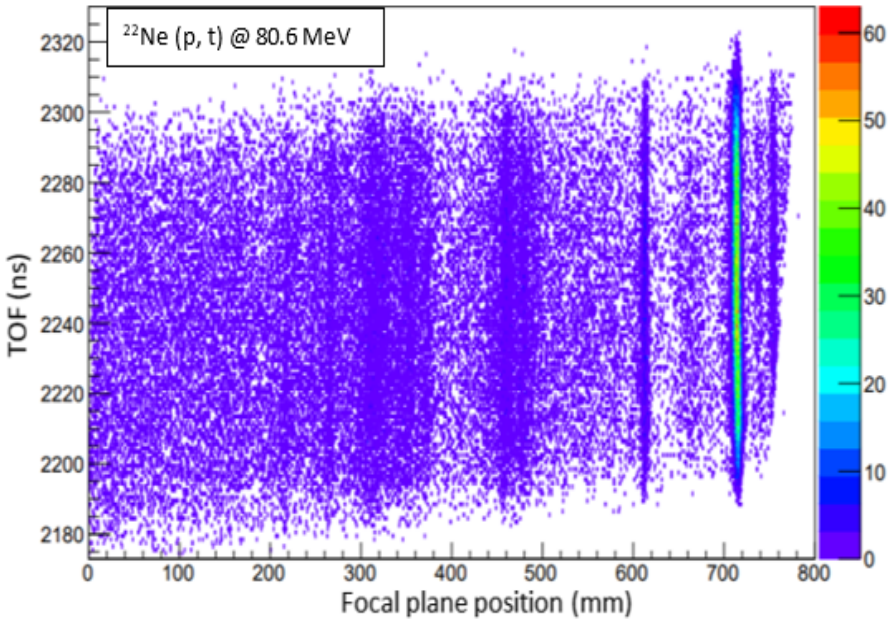

Figure 4.10: A scatterplot of the TOF vs X1 position for the ^{22}Ne(p,t) reaction at zero degrees, with line shape correction.

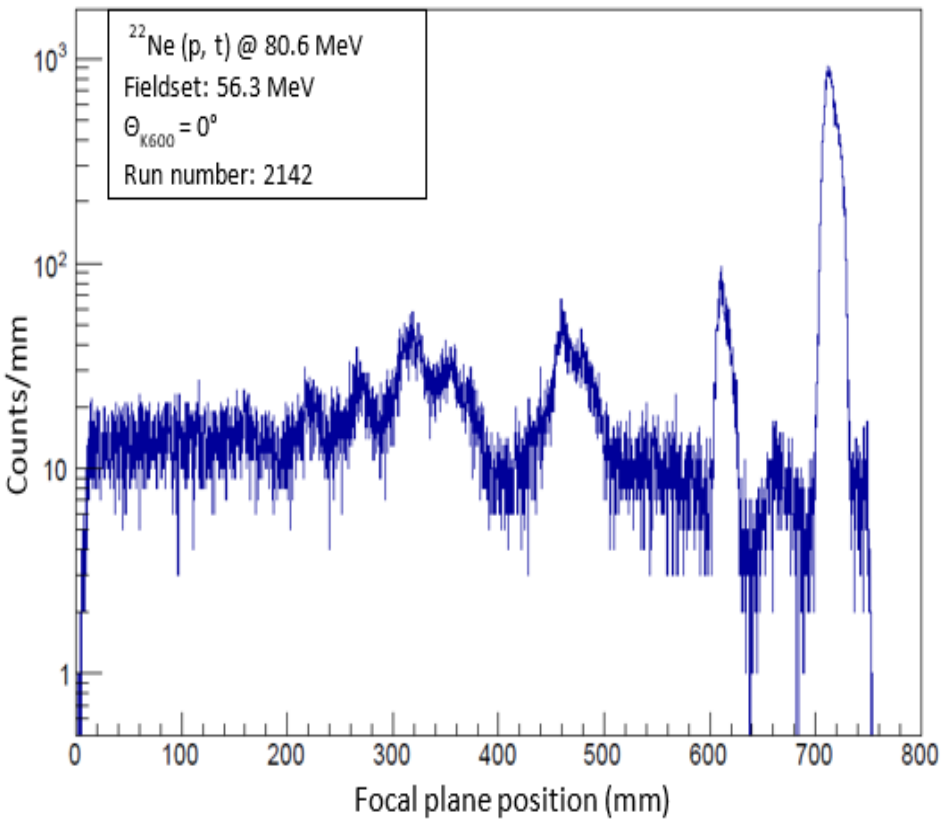

Figure 4.11: Measured X1 position spectrum, without line shape correction.

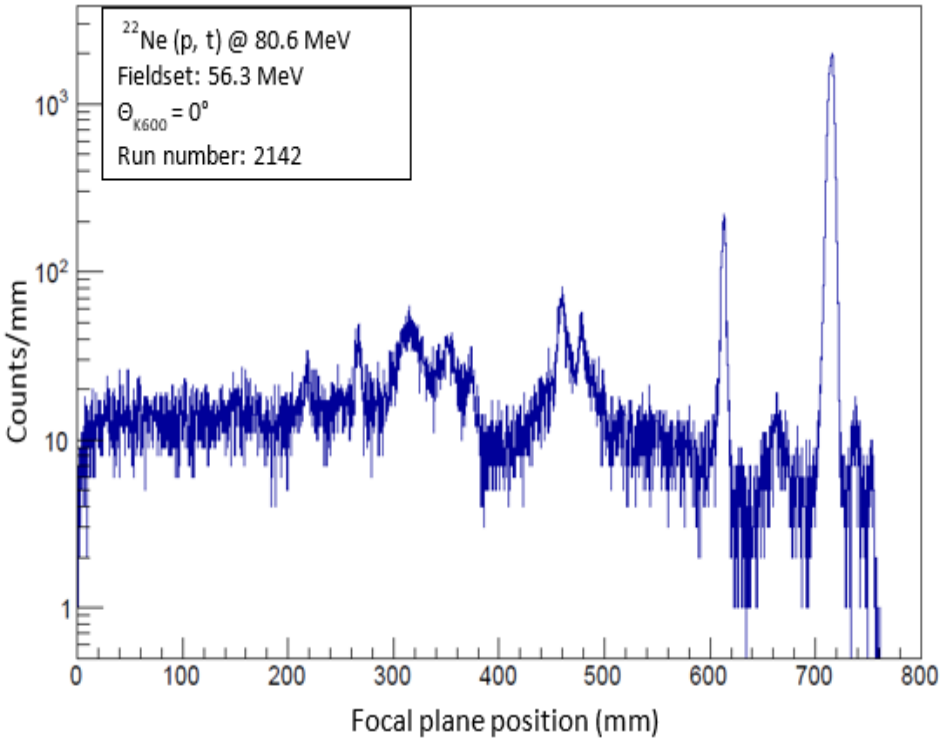

Figure 4.12: The X1 position spectrum, with line shape correction.

4.6 Position offsets

During the data acquisition period there were slight variations in beam energy caused by RF adjustments at the SSC as operators tried to keep the required beam intensity constant. This led to slight position shifts seen in the position spectra of different runs relative to each other. This should be corrected for since different runs were added together in the final analysis. The other reason that position offsets were corrected for was to avoid severe degredation of the experiment's resolution.

The position offsets were determined for each run, relative to a reference run number 2142. In each run, the peak of the ^{10}C ground state in the position spectrum was fitted with a function that consisted of a sum of a Gaussian peak and a first order polynomial. The centroid of the Gaussian was taken to be the peak position, and this peak position was determined for all the relevant data runs. The obtained position offsets with respect to run number 2142 are shown Table 4.2, and they were used by the analysis code for further analysis. Figures 4.13 and 4.14 show the position spectra for all neon data before and after the position correction, respectively.

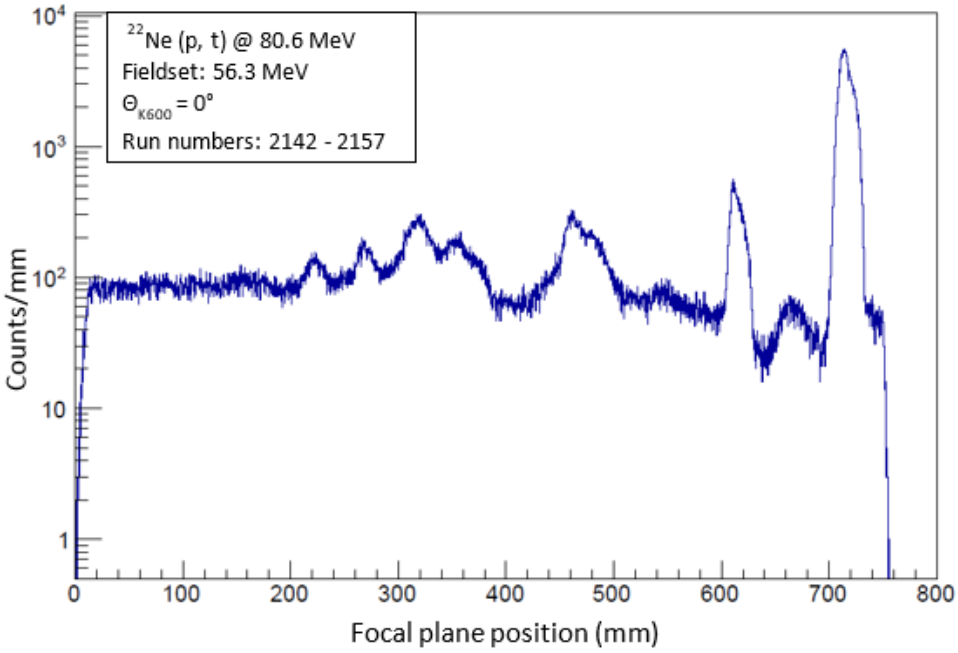

Figure 4.13: PID selected position spectrum for the ^{22}Ne(p,t) reaction for runs 2142 - 2157 without taking position offsets into account.

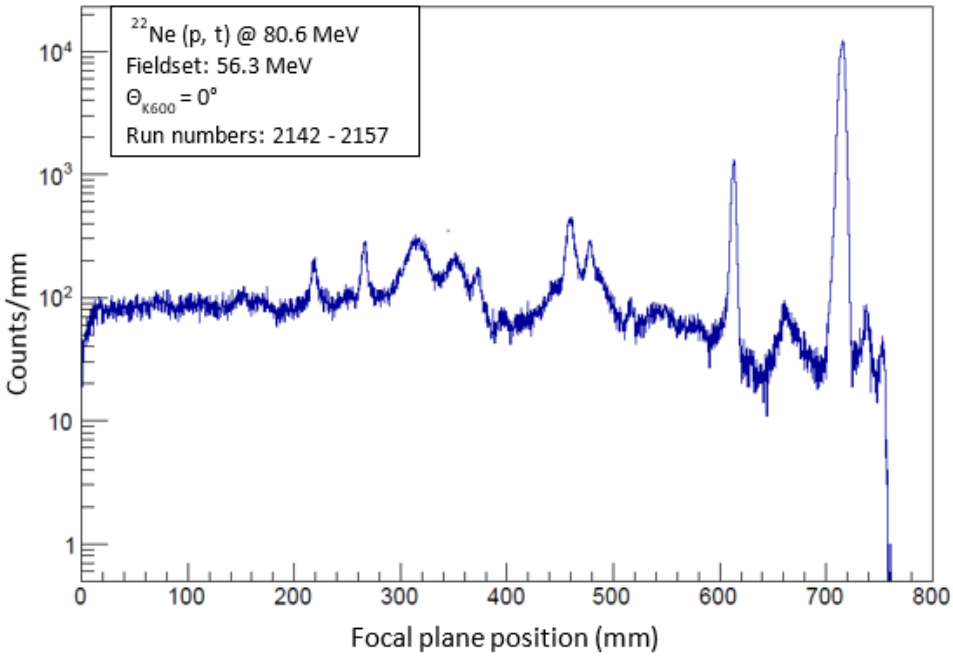

Figure 4.14: PID selected position spectrum for the ^{22}Ne(p,t) reaction for runs 2142 - 2157 with position offsets taken into account.

Table 4.2: Position offsets for all the runs with respect to Ne run 2142, the reference run.

Run No.	Clock time	Day	Offsets (mm)
2142	18:31 - 19:36	Sunday	0
2132	12:23 - 12:53	Sunday	3.13
2137	14:36 - 15:07	Sunday	3.58
2140	16:24 - 16:31	Sunday	1.15
2141	16:32 - 16:59	Sunday	5.36
2143	19:38 - 20:04	Sunday	1.04
2145	20:09 - 21:09	Sunday	1.17
2147	21:15 - 22:16	Sunday	4.09
2148	22:17 - 22:40	Sunday	1.31
2151	22:58 - 23:56	Sunday	1.43
2152	23:58 - 00:25	Sunday	1.39
2154	00:38 - 01:10	Monday	4.03
2155	01:39 - 02:38	Monday	0.95
2156	02:40 - 03:41	Monday	1.18
2157	03:40 - 04:37	Monday	1.68
2165	05:14 - 06:00	Monday	1.13

4.7 Energy calibration procedure

The first four states of ^{10}C (g.s, 3.35 MeV, and 5.22 and 5.38 MeV), and the 16.73 MeV ^{20}Ne state were identified in the position spectrum, as shown in Fig. 4.15. The ^{10}C peaks were identified with the aid of the aramid spectrum shown in Fig. 4.16. From the focal plane position spectrum, the peak position for each state was determined. A two-body kinematics program (Jrelkin) for relativistic kinematic calculations was then used to calculate the rigidity values associated with each state, taking into account the thickness of the target (^{22}Ne gas), which was estimated to be 1.6 mg/cm^2. Table 4.3 summarizes the values collected.

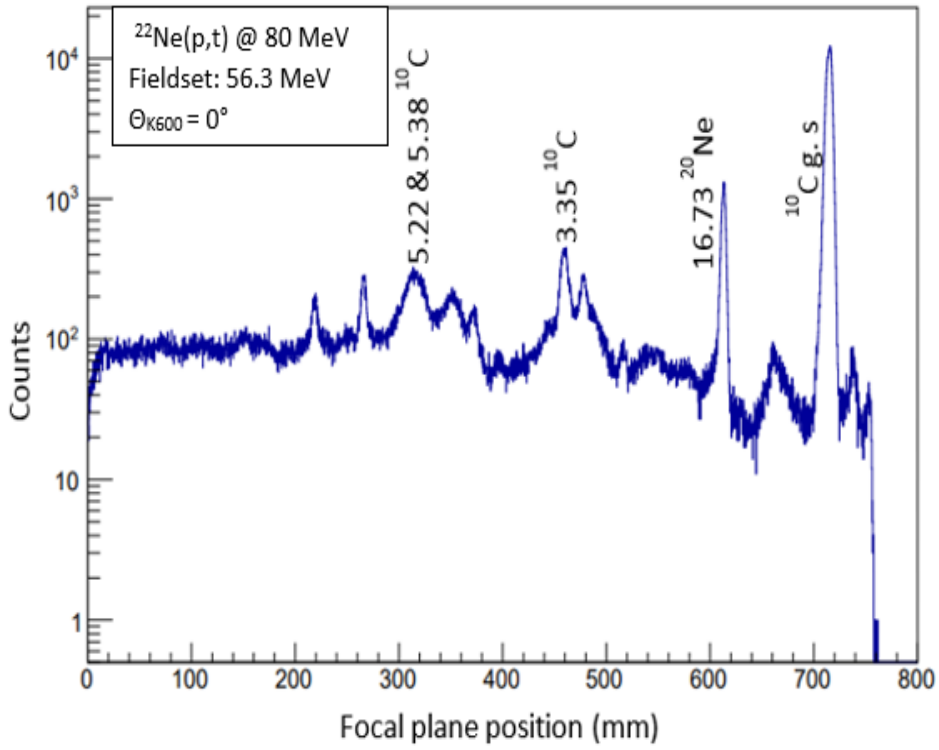

Figure 4.15: Focal plane position spectrum for the ^{22}Ne gas target showing three states of ^{10}C and the 16.73 MeV ^{20}Ne state.

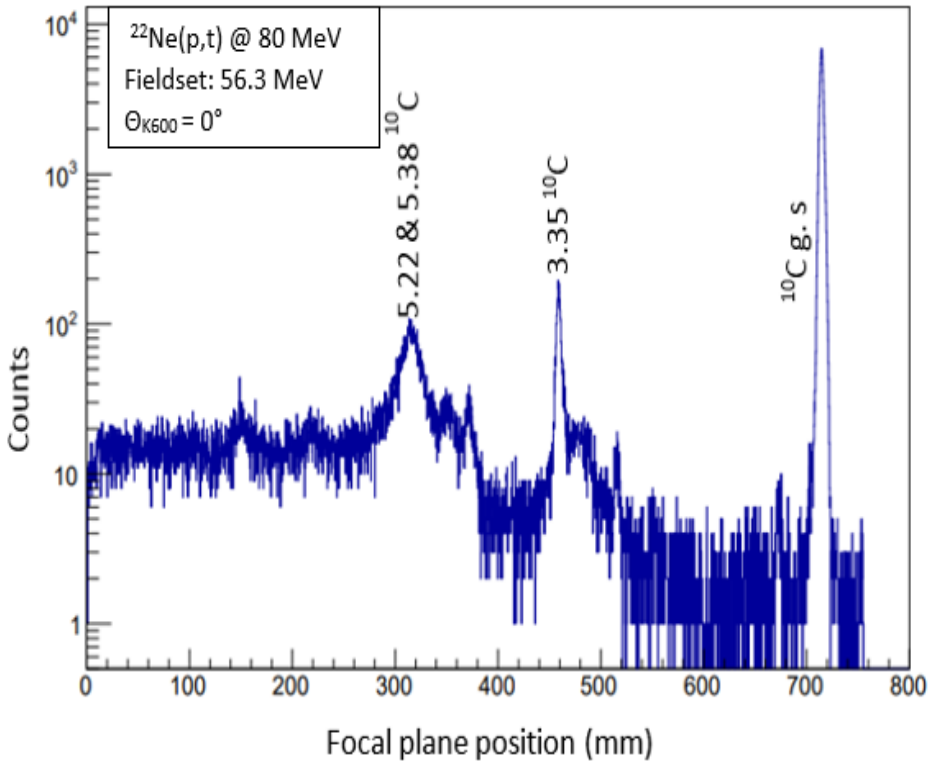

Figure 4.16: Focal plane position spectrum for the aramid showing ^{10}C states.

Table 4.3: States selected for energy calibration. The value 5.30 MeV represents the average of the 5.22 MeV and 5.38 MeV ^{10}C states.

States (MeV)	Peak position (mm)	Rigidity
^{10}C g.s	715.5	1866.8060
16.73 ^{20}Ne	613.0	1845.515
3.55 ^{10}C	459.4	1813.4435
5.30 ^{10}C	315.0	1791.3040

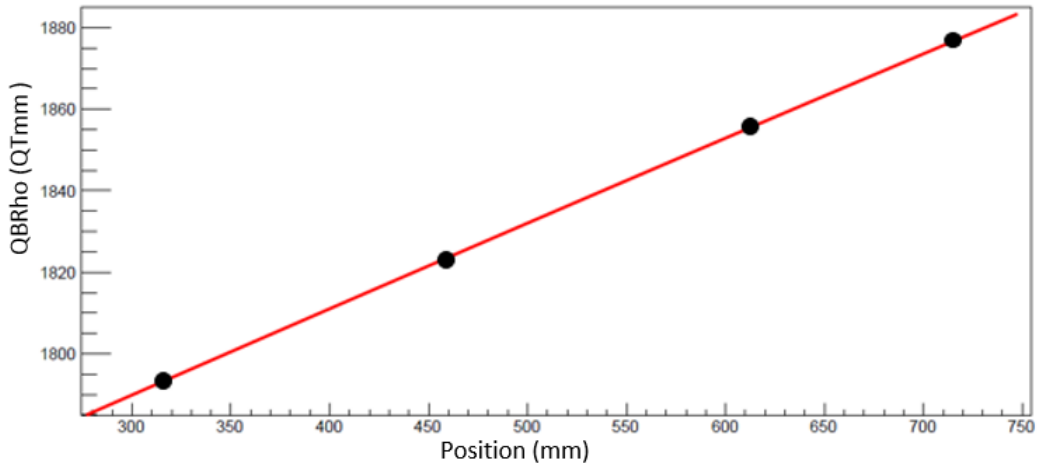

Figure 4.17: The second order polynomial relationship between rigidity and peak position obtained when using ^{10}C states and one ^{20}Ne state.

From the obtained rigidity values and the peak positions for each state, the plot of rigidity versus peak position is generated as shown in Fig. 4.17. The plot enables an extraction of rigidity for any position. Momentum of the particles (in this case tritons) is then obtained from the extracted rigidity using

$$\frac{P_{\mathrm{t}}}{q} = QB\rho \times c, \tag{4.3}$$

where P_{t} is the momentum of tritons, q is the charge, $QB\rho$ is the magnetic rigidity, and c is the speed of light.

The kinetic energy of tritons is then calculated from the momentum using

$$E_{\mathrm{t}} = \sqrt{P_{\mathrm{t}}^2 + m_{\mathrm{t}}^2} - m_{\mathrm{t}}, \tag{4.4}$$

where E_{t} is the kinetic energy of the tritons, P_{t} is the momentum of the tritons and m_{t} is the mass of the tritons.

Finally, the triton kinetic energy is converted into excitation energy E_{x} using the equation for two-body kinematic reactions:

$$E_{\mathrm{x}} = E_{\mathrm{b}} - E_{\mathrm{t}} - E_{\mathrm{r}} + Q. \tag{4.5}$$

where E_{b}, E_{t} and E_{r} are the kinetic energies of the beam, triton and recoil particle, respectively, and Q is the Q-value for the reaction.

4.8 Background subtraction

The use of the gas cell (described in Section 3.3) has resulted in the contamination of the ^{20}Ne excitation energy spectrum measured using the ^{22}Ne(p,t)^{20}Ne reaction with peaks from other reactions. The gas cell has windows that are made of aramid. Aramid consists of $C_{14}O_2N_2Cl_2H_8$ molecules. The reactions ^{12}C(p,t)^{10}C, ^{16}O(p,t)^{14}O, and ^{14}N(p,t)^{12}N from the aramid foils are responsible for contamination of the ^{20}Ne excitation energy spectrum. However, ^{14}N and ^{16}O could also get into the target due to an air leak since they are also found in air. Figure 4.18 shows the aramid excitation energy spectrum. The aramid background is complicated by the fact that it is created by two different foils separated by a gas at 1.3 bar.

The effect of the differences in energy loss of different particles (protons and tritons) moving through the ^{22}Ne gas must be taken into account in order to make an accurate background subtraction. Figure 4.19 illustrates the two different scenarios that lead to a difference in energy loss by protons and tritons, for the reactions that contaminate the ^{20}Ne excitation energy spectrum. Tritons will lose more energy in the ^{22}Ne gas than protons since

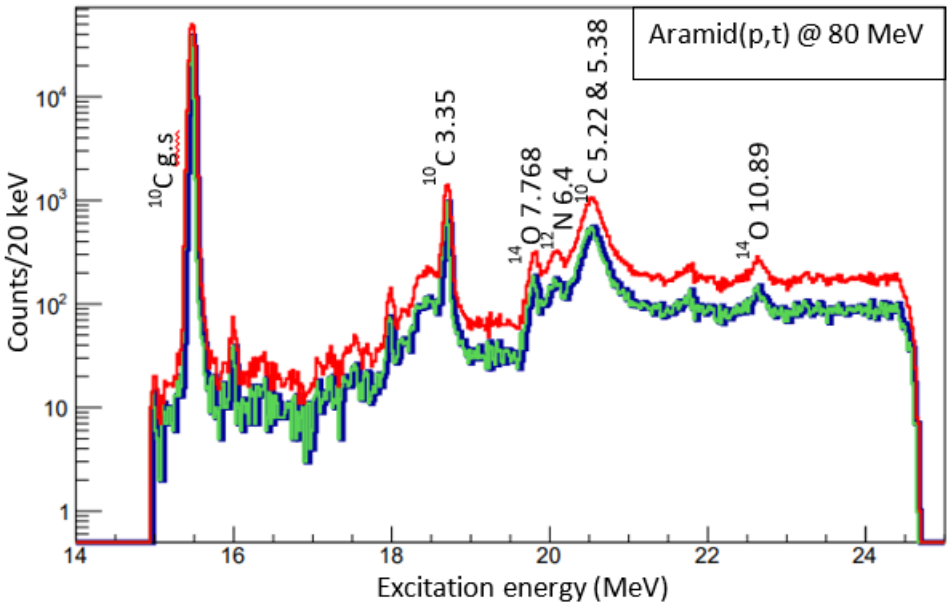

Figure 4.18: The excitation energy spectrum for the background data at zero degrees. The green spectrum is the background data plot for the back foil, whereas the blue one is the plot for the front foil. The red spectrum is the sum of back and front foil.

they have higher mass, and they traverse with lower energy due to the high negative Q-value of the ^{22}Ne(p,t)^{20}Ne reaction. Therefore, tritons originating from the first foil will reach the focal plane with lower triton momenta because of the greater energy loss of tritons compared to protons. This causes a broadening of the contaminant peaks, and may in severe cases result in visible double-peaking.

In this study, the energy loss of the different particles moving through the ^{22}Ne gas was determined by considering the occurence of double peaking. These double peaks are approximately 40 keV apart. This effect is illustrated in Fig. 4.20, for the case of the ground state of ^{10}C. The 40 keV value was obtained by determining the mean energy of (p,t) events from the front foil and (p,t) events from the back foil. The mean energies for the front foil and back foil were found to be located at 15.495 MeV and 15.455 MeV, respectively. A 40 keV mean energy difference is yielded.

The front foil and the back foil spectra were summed together to produce the red spectrum as shown in Fig. 4.18. This new spectrum was then smoothed, i.e. each peak was made broader so that the width due to energy straggling in the ^{22}Ne gas can be considered. The broader peaks from aramid background

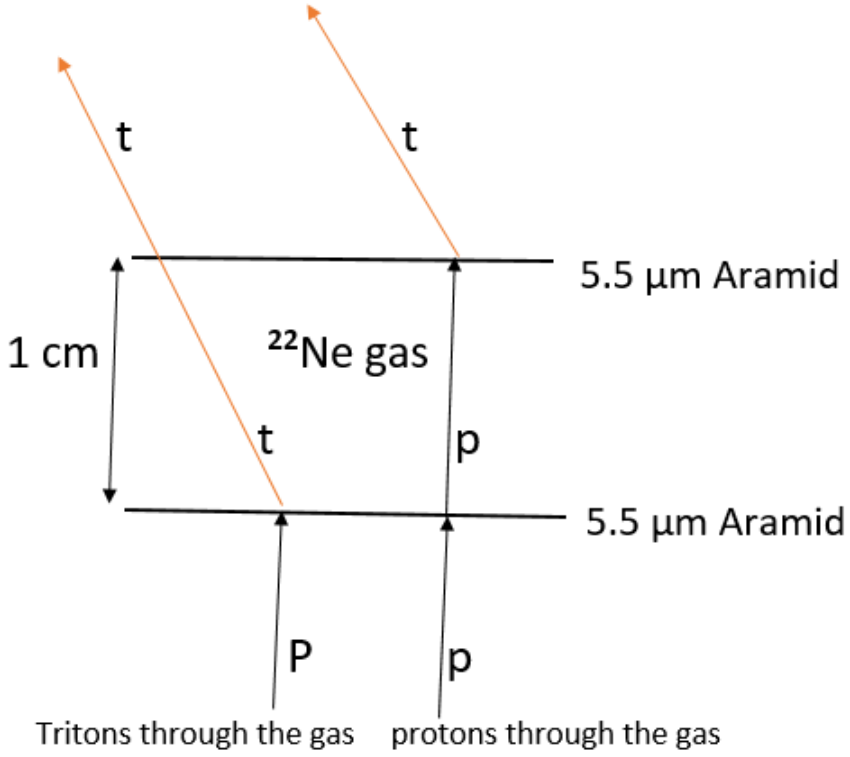

Figure 4.19: Different scenarios of the ^{12}C(p,t)^{10}C reaction with either protons or tritons moving through ^{22}Ne gas.

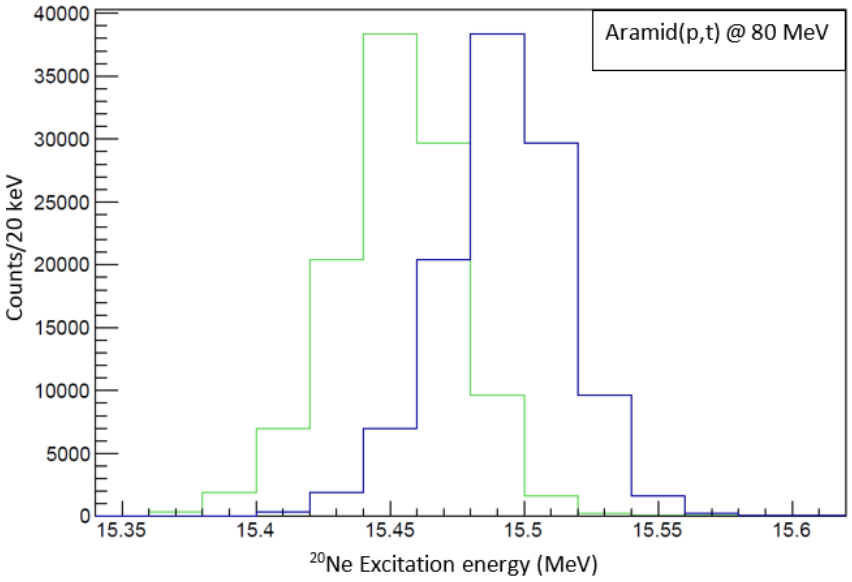

Figure 4.20: Double peaking effect for the case of the ground state of ^{10}C. The green peak represents the back foil scenario whereas the blue one represents the front foil scenario.

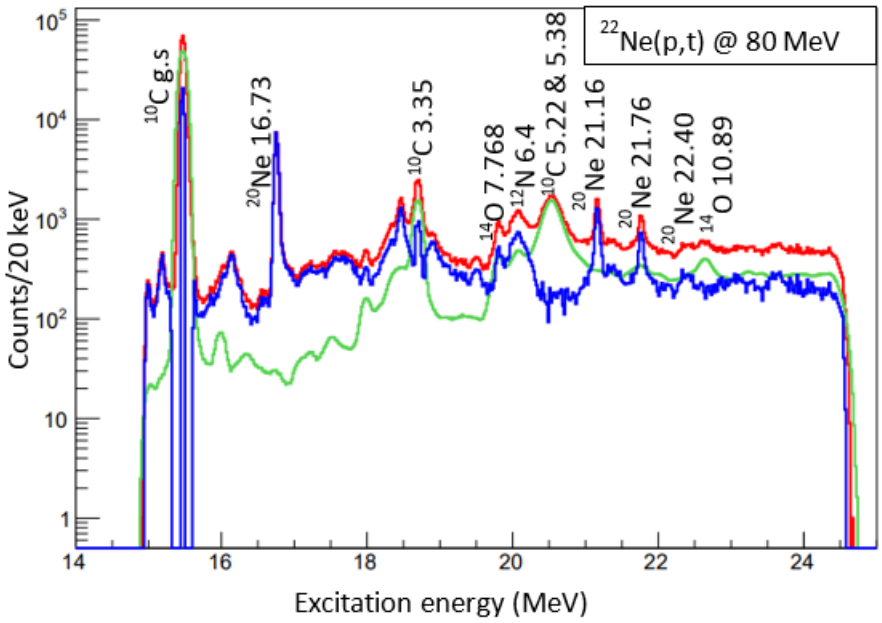

Figure 4.21: The excitation energy spectrum for the ^{22}Ne(p,t) reaction at zero degrees. The red spectrum is the ^{22}Ne gas spectrum, and the green one is the sum of the background data. The blue spectrum is the background subtracted spectrum.

spectrum were then normalized to the ^{20}Ne data by taking into consideration the proton beam charge observed during data collection with the ^{22}Ne gas target and with the aramid background measurements. Figure 4.21 shows the ^{22}Ne and aramid data. Figure 4.22 shows the background subtracted result of ^{22}Ne(p,t) spectrum. The structures around 18.68 MeV and 20.50 MeV are remnants of the ^{10}C and they are caused by the artefacts from the background subtraction procedure (described in the text above). The peaks around 19.82 MeV and 20.07 MeV are states from ^{14}O and ^{12}N, respectively, and they could partially be due to air leaks in the gas cell. The 22.4 MeV state seen is weaker than the 22.5 MeV state as seen in Ref. [Swa15]. There is a potential state of some nature at $E_{\mathrm{x}} = 23.68$ MeV.

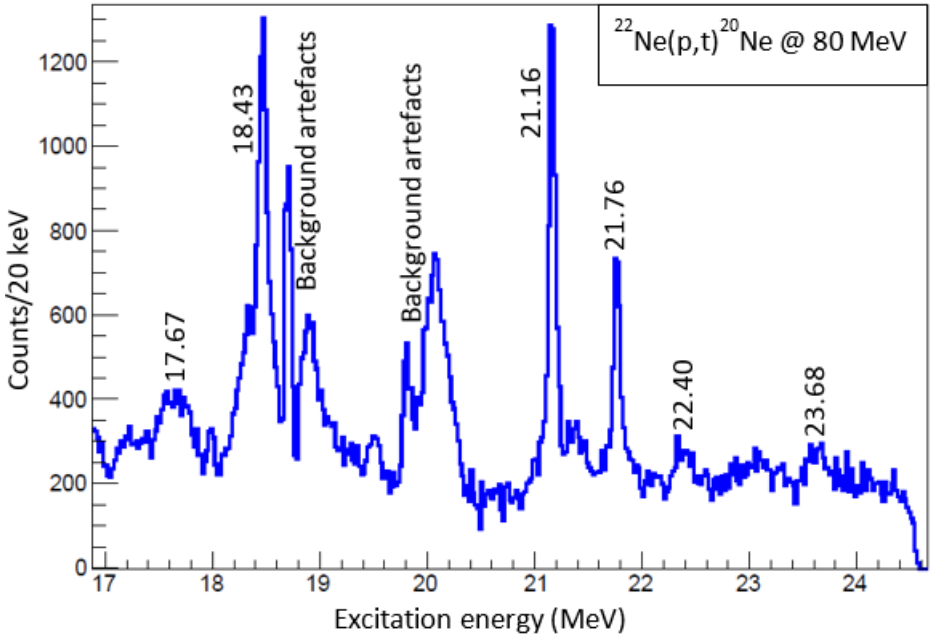

Figure 4.22: Aramid subtracted excitation energy spectrum showing observed states (labeled) in ^{20}Ne.

4.9 Experimental cross-sections

The experimental double differential cross-section with units mb/srMeV is calculated using the following equation:

$$\frac{d^2\sigma}{d\Omega dE} = \frac{N_\mathrm{c}}{I_\mathrm{f} \times \rho \times D \times \varepsilon \times \Delta\Omega \times \Delta E}, \tag{4.6}$$

where N_c represents the number of events per energy bin, I_f is the particle flux of the incident beam upon the target, ρ is the number of target nuclei per unit area, D is the electronic dead time correction factor, ε is the VDC efficiency, $\Delta\Omega$ is the K600 solid angle, and ΔE is the energy bin size.

The number N_c was determined for each individual state by performing a Gaussian fit over the peak in the excitation energy spectrum and determining the area of the peak by using the equation for a continuous Gaussian distribution as shown below

$$\int_{-\infty}^{\infty} Ce^{\frac{(x-\bar{x})^2}{2\sigma^2}} dx = C\sigma\sqrt{2\pi}, \tag{4.7}$$

where σ represents the standard deviation as determined in the fit and $FWHM = 2.35 \times \sigma$, C represents the amplitude, and $\bar{x}$ is the mean value of the peak.

The incident flux of projectiles is determined using

$$I_{\mathrm{f}} = \frac{CII \times R}{e}, \tag{4.8}$$

where CII is the current integrator scaler reading, R represents a range that was set on the current integrator (in nA), and e is the charge of a single proton beam particle (in Coulombs).

The number of target nuclei per unit area is determined as

$$\rho = \frac{\lambda \times N_{\mathrm{A}}}{A}, \tag{4.9}$$

where N_A represents the Avogadro constant, λ is the target thickness in mg.cm^{-2} and A is the mass number of the target nucleus.

The solid angle used is 3.95×10^{-3} steradians (sr) and is calculated using

$$\Delta\Omega = \frac{\Delta A}{d^2} = \frac{\pi \times r^2}{d^2}, \tag{4.10}$$

where r is the radius of the collimator and d is the distance between the target and the collimator.

The extracted cross-sections calculated using Eq. (4.6) integrated with respect to ΔE and the widths for the states observed in ^{20}Ne (see Fig. 4.22) for the present study are shown in Table 4.4. The cross section for each peak was found through fitting a Gaussian plus a polynomial background on that particular peak as shown in Figs. 4.23 and 4.24 where a state of interest (22.4 MeV) was fitted, and its area was determined using the Gaussian peak area formula. Figures 4.23 and 4.24 represent the ^{22}Ne gas target data before background

subtraction and after background subtraction, respectively. These figures show that before and after the background subtraction process there is a clear peak close to 22.5 MeV. The cross-section errors were determined by considering percentage contributions for the sum of the statistical error for each peak plus the experimental systematic error, which is estimated to be 10%.

Table 4.4: Cross sections and widths (FWHM) for the states observed in ^{20}Ne in Fig. 4.22.

Excitation energy (MeV)	Spin and parity	Cross section (μb/sr)	FWHM (keV)
17.67	2^+	15.4±1.9	353
18.43	2^+	14.8±2.0	75
21.16	0^+	26.0±3.2	82
21.76	1^-	14.0±2.1	44
22.40	0^+	10.0±1.7	235
23.68	9^-	8.98±1.2	234

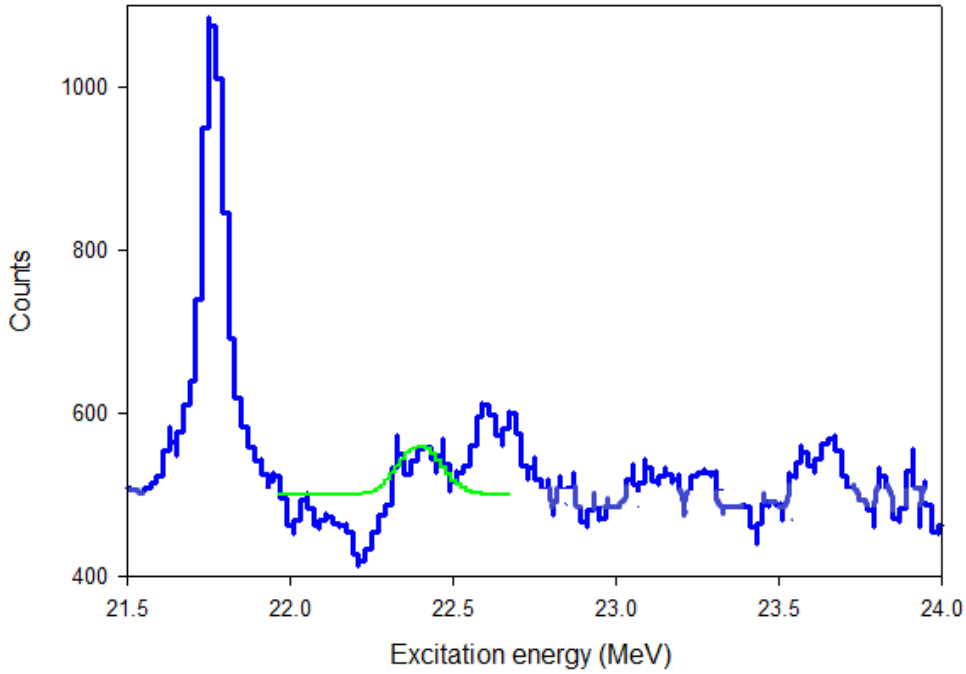

Figure 4.23: An example of how the peaks were fitted using Gaussian (green colour) on the ^{22}Ne gas target data before background subtraction.

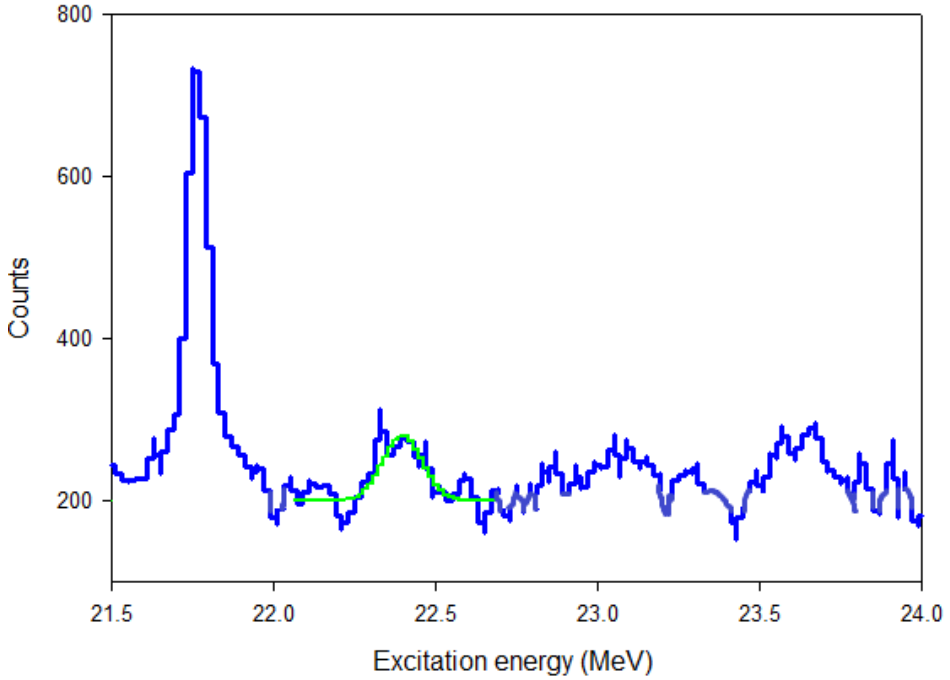

Figure 4.24: An example of how the peaks were fitted using Gaussian (green colour) on the ^{22}Ne gas target data after background subtraction.

4.10 Comparison of $E_{\mathrm{p}} = 80$ and $E_{\mathrm{p}} = 60$ MeV data

Comparison of the present dataset at $E_{\mathrm{p}} = 80$ MeV with the data at $E_{\mathrm{p}} = 60$ MeV from Refs. [Swa14, Swa15] shown in Fig. 4.25, was performed in terms of the excitation energy spectrum. This was done with the purpose of showing whether the state found at $E_{\mathrm{x}} = 22.4$ MeV in the present data is the same as the state found at $E_{\mathrm{x}} = 22.5$ MeV in Ref. [Swa15], by comparing the present data and data used in Ref. [Swa15] as shown in Fig. 4.26. The $E_{\mathrm{x}} = 21.76$ and 22.4 MeV states in the present study were shifted up in excitation energy to match the $E_{\mathrm{x}} = 21.80$ and 22.5 MeV states for the $E_{\mathrm{p}} = 60$ MeV data, in order to do comparison with wavelet-based semblance analysis. The same data were scaled up by a factor of 1.5 with the purpose of overlaying it with the $E_{\mathrm{p}} = 60$ MeV data. Figure 4.26 shows that the two datasets are compatible.

The wavelet-based semblance analysis (described in Section 2.2.3) was performed with the purpose of proving compatability of the two datasets as shown in Fig. 4.26, especially for the state at $E_{\mathrm{x}} = 22.5$ MeV. The two-dimensional wavelet coefficient plot of the two dataset were compared, and the maximum scale was restricted to 1000 keV in order to show the detail of subtructures existing at smaller energy scales. This is illustrated in Fig. 4.27 (b) and (d).

It is clear from the two-dimensional wavelet coefficient plots in Fig. 4.27 (b) and (d) that the states observed in the present data except at $E_{\mathrm{x}} = 19.82$ MeV and $E_{\mathrm{x}} = 20.07$ MeV, are also observed in the $E_{\mathrm{p}} = 60$ MeV data. They are represented by red and yellow colours and they both imply positive correlation. In particular, at a scale of 600 keV (peak width 300 keV, see Section 2.2) at $E_{\mathrm{x}} = 22.5$ MeV in Fig. 4.27 (b) and (d), a structure represented by a yellow colour which implies positive correlation indicates a tentative state. This state also presents a good agreement in the semblance plot projection shown in Fig. 4.27 (f), which indicates a maximum semblance of about 0.5 at a scale of 600 keV, implying a positive correlation.

Moreover, in Fig 4.27 (b) and (d) at the same excitation energy $E_{\mathrm{x}} = 22.5$ MeV, substructures are seen at scales of about 400 keV and 200 keV which

are also represented on Fig. 4.27 (f) by a maximum semblance of 0.2 and 0.8, respectively. Therefore, these substructures and a structure at 600 keV could indicate a possibility of two peaks at $E_x = 22.5$ MeV, however, more counting statistics are needed to investigate this further.

Cross sections were compared and extracted cross-sections for the states observed in the ^{20}Ne nucleus above $E_x = 21$ MeV, for the present data at $E_p = 80$ MeV and data obtained with $E_p = 60$ MeV [Swa15] are shown in Table 4.5.

Table 4.5: Comparison of cross-sections ($\frac{d\sigma}{d\Omega}$) for the states observed in ^{20}Ne above $E_x = 21$ MeV at $E_p = 80$ MeV and $E_p = 60$ MeV. Data(80) represents the present data and Data(60) represents the data used in Ref. [Swa15].

Data(80) E_x (MeV)	Data(60) E_x (MeV)	Data(80) $\frac{d\sigma}{d\Omega}$ (μb/sr)	Data(60) $\frac{d\sigma}{d\Omega}$ (μb/sr)
21.16	21.16	26.0±3.2	38±9
21.76	21.80	14.4±2.1	11±2.6
22.40	22.50	10.0±1.7	22±4.9

The cross-section values determined in the present data are lower than the ones determined in the $E_p = 60$ MeV data. However, the cross-section values for the states at $E_x = 21.16$ MeV and $E_x = 21.76$ MeV in the present dataset fall within the cross-section error bars of the states at $E_x = 21.16$ MeV and $E_x = 21.80$ in the $E_p = 60$ MeV data.

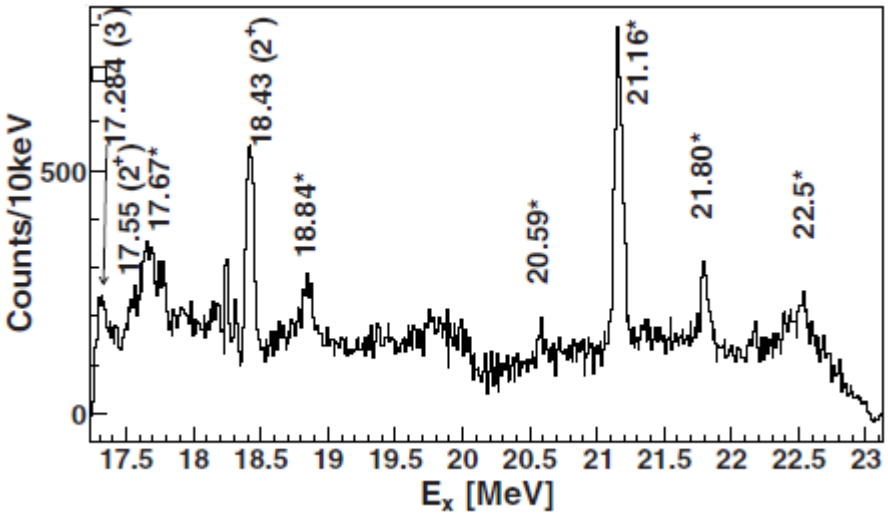

Figure 4.25: Excitation energy spectrum for the ^{22}Ne(p,t)^{20}Ne reaction at $E_{\mathrm{p}} = 60$ MeV (taken with permission from [Swa15]).

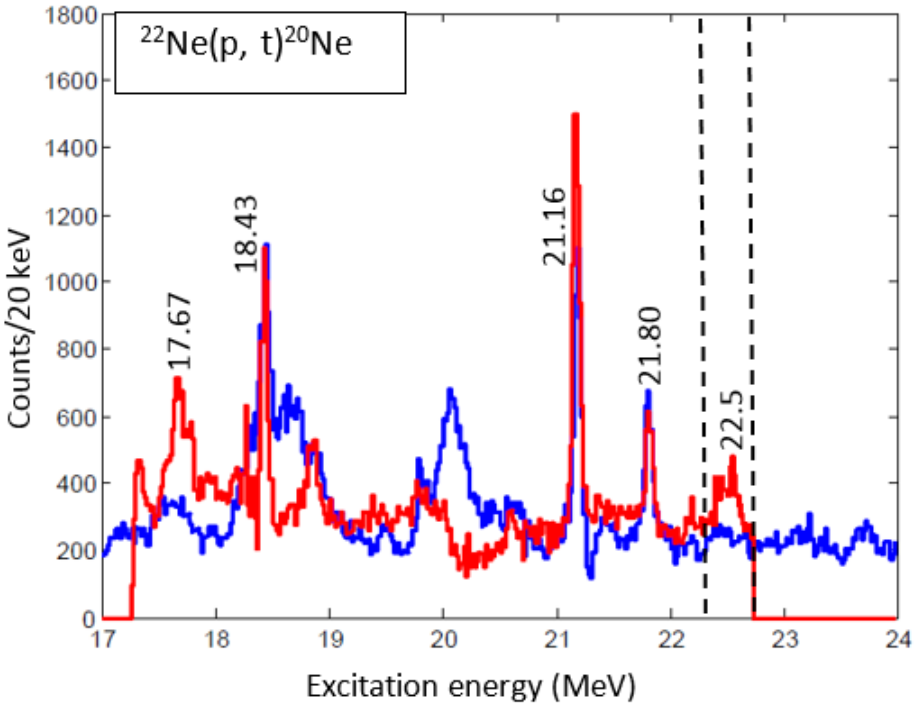

Figure 4.26: Comparison of present data at $E_{\mathrm{p}} = 80$ MeV with data from [Swa15] at $E_{\mathrm{p}} = 60$ MeV for the ^{22}Ne(p,t)^{20}Ne reaction. The blue spectrum represents the excitation energy spectrum for the present data and the red spectrum represents the excitation energy spectrum for the $E_{\mathrm{p}} = 60$ MeV data. The vertical dashed lines indicate the region of interest.

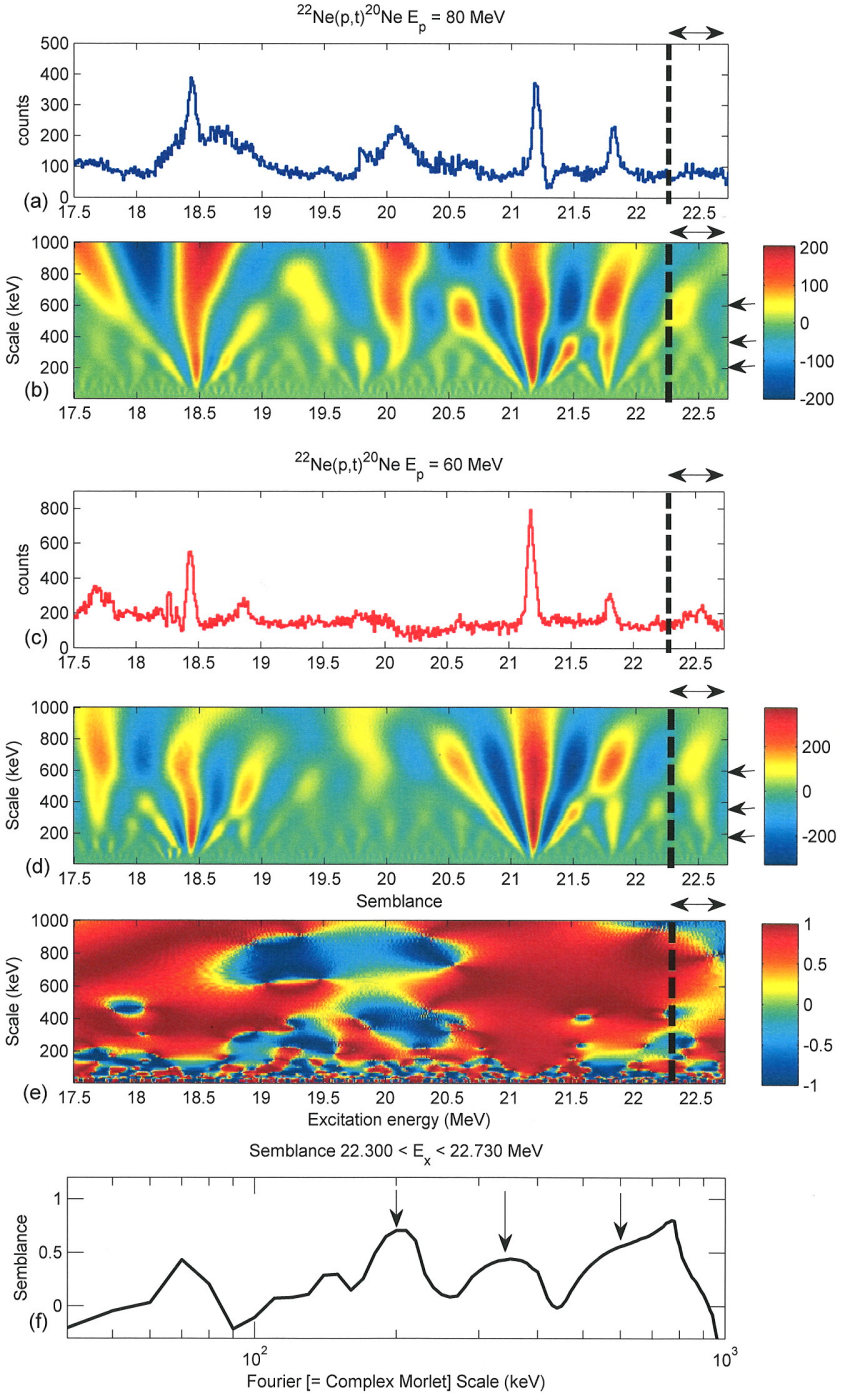

Figure 4.27: (a) Excitation energy spectrum for the present data, and (b) its two-dimensional wavelet coefficient plot. (c) Excitation energy spectrum for the $E_{\mathrm{p}} = 60$ MeV data, and (d) its two-dimensional wavelet coefficient plot. Red and blue in the two-dimensional wavelet coefficient plots represent positive and negative scale values, respectively. (e) Semblance plot of comparison of b and d showing the correlation between the two data sets. (f) Semblance plot projection for the region around $E_{\mathrm{x}} = 22.5$ MeV which is the region of interest.

4.11 Discussion

The present study, which investigated the ^{20}Ne nucleus particularly at $E_x = 22.5$ MeV, with $E_p = 80$ MeV at zero degrees using the ^{22}Ne(p,t)^{20}Ne reaction, displays states observed in Ref. [Swa15]. Figure 4.22 shows ^{20}Ne states produced in this study, which do not include the states at $E_x = 18.68$ MeV and $E_x = 20.50$ MeV where there are the remnants of ^{10}C states caused by the imperfect background subtraction procedure (described in Section 4.8) followed. The peaks around 19.82 MeV and 20.07 MeV are states from ^{14}O and ^{12}N, respectively, and they could partially be due to small air leaks in the gas cell.

Three states found by Swartz *et al.* [Swa15] above $E_x = 21$ MeV are also seen in this study at $E_x = 21.16$, 21.76 and 22.4 MeV with widths of 82 keV, 44 keV and 235 keV, respectively. In Ref. [Swa15] the state found at $E_x = 22.5$ MeV with a width of 260 keV was proposed to be a tentative candidate for the 5-alpha cluster state [Swa14, Swa15]. Its width is comparable to the 235 keV width for the state at $E_x = 22.4$ MeV found in the present study. Another state of unknown nature is observed at $E_x = 23.68$ MeV and has a width of 234 keV.

The observed state at $E_x = 22.4$ MeV lies at 3.23 MeV above the 5α break-up threshold [EXF98]. This state lies very close to a tentative 5α cluster candidate from Ref. [Swa15]. The state observed at $E_x = 22.4$ MeV is assumed to be the same as the state found at $E_x = 22.5$ MeV in Ref. [Swa15] as shown in Fig. 4.26.

Figure 4.27 shows a comparison of the $E_p = 60$ MeV data and the present data with wavelet-based semblance analysis, and a positive correlation represented by the red and yellow colours on the two-dimensional wavelet coefficient plots (see Fig. 4.27 (b) and (d)), between the states is observed, except at $E_x = 19.82$ MeV and $E_x = 20.07$ MeV. Those states are not produced with $E_p = 60$ MeV since they are artefacts of the background subtraction procedure which could not be eliminated at 80 MeV. These peaks are states from ^{14}O and ^{12}N, respectively, and they could be due to air leaks into the gas cell.

Around the region of interest ($E_x = 22.5$ MeV) which is represented by a

scale of 600 keV (noting that half the scale value represents FWHM of a corresponding peak) on Fig. 4.27 (b) and (d), a positive correlation shown by a maximum semblance of 0.5 on the semblance projection plot in Fig. 4.27 (f). This implies that a state seen at $E_x = 22.5$ MeV in the $E_p = 60$ MeV data is also seen in this study. Substructures are observed also at the the same excitation energy ($E_x = 22.5$ MeV) at a scales of about 400 keV and 200 keV with a maximum semblance of about 0.2 and 0.5, respectively, and this could indicate that the state at $E_x = 22.4$ MeV consists of two peaks, as was also speculated in Ref. [Swa14].

Finally, in the present study, the cross sections for all the states observed in ^{20}Ne were determined, and are shown in Table 4.4. The cross-section values for the states found above $E_x = 21$ MeV (21.16, 21.76 and 22.4 MeV) were compared to the ones determined at $E_p = 60$ MeV as shown in Table 4.5. The cross section values found in the present study are smaller than the cross section values obtained in the $E_p = 60$ MeV because of the higher beam energy of 80 MeV, which is physically less conducive to populating low-spin states. It was found that the cross section values for the states $E_x = 21.16$ MeV and $E_x = 21.76$ MeV fall within the cross-section error bars for the states at $E_x = 21.16$ MeV and $E_x = 21.80$ MeV in Ref. [Swa15]. This study also suggests the existence of a 22.4 MeV state in ^{20}Ne. The fact that its cross section is lower at $E_p = 80$ MeV than at $E_p = 60$ MeV is consistent with it being a 0^+ state. However, in order to better understand it further experimental work is required to measure an angular distribution with counting statistics better than the present measurement.

Chapter 5

Conclusions and future work

5.1 Conclusions

A measurement to investigate if another study can identify a state seen at $E_x = 22.5$ MeV in the $E_p = 60$ MeV data [Swa15] was performed with a proton beam of energy $E_p = 80$ MeV using the ^{22}Ne(p,t)^{20}Ne reaction. States produced with $E_p = 60$ MeV data are also seen with $E_p = 80$ MeV, at $E_x = 17.67$ MeV, $E_x = 21.16$ MeV, $E_x = 21.76$ MeV and $E_x = 22.4$ MeV. A state of unknown nature is produced at $E_x = 23.68$ MeV.

A tentative candidate for the 5-α cluster state seen previously is also identified at $E_x = 22.4$ MeV with a width of 235 keV, which is comparable to the 260 keV width of the stronger $E_x = 22.5$ MeV state found at $E_p = 60$ MeV. Furthermore, its cross-section value of 10.0 ± 1.7 μb/sr, which is smaller than the cross-section value of the state at $E_x = 22.5$ MeV in the $E_p = 60$ MeV data possibly due to a momentum mis-match. This is because the ^{22}Ne(p,t)^{20}Ne reaction will have a lower cross section at small angles with this higher beam energy. However, even though the experimental conditions were not ideal for finding a 0^+ state, the wavelet-based semblance analysis does suggest that there is a state at $E_x = 22.5$ MeV. It also suggests substructures which may be indicative of two peaks around 22.5 MeV, something which there were also indications of in Ref. [Swa14]. This is the second experiment which indicates the presence of a state at and/or around 22.5 MeV in ^{20}Ne.

5.2 Future work

More experimental data are needed to investigate the higher excitation region of ^{20}Ne. A candidate for the 5-alpha cluster state was excited through the (p,t) reaction at $E_{\mathrm{p}} = 60$ MeV and $E_{\mathrm{p}} = 80$ MeV. In the future more experiments with longer counting times must be performed to characterise this state in terms of a measured angular distribution to determine the spin and parity. Decay modes of the state can also be investigated in order to see if indeed it is a candidate for the 5α-cluster state above the 5-alpha break-up threshold. One may also investigate the ^{22}Ne(p,^{3}He)^{20}F data to confirm whether we have indeed observed a $T = 0$ state.

References

[Ban76] H. Bando. In: *Nucl. Phys. A* 261 (1976), pp. 269–281.

[Ber77] W. Bertozzi, M. Hynes, C. Sargent, C. Creswell, P. Dunn, A. Hirsch, M. Leitch, B. Norum, F. Rad, and F. Sasanuma. In: *Nuclear Instrumentation Methods* 141 (1977), pp. 457–476.

[Bro18] Bronkhorst. *Bronkhorst Products*. 2018 (accessed March 2, 2018). URL: `https://www.bronkhorst.com/products/`.

[Cen16] N. N. D. Center. "Nuclear Science References (version from 2016), information extracted from the NSR database". In: (2016). URL: `http://www.nndc.bnl.gov/ensdf`.

[Che07] M. Chernykh, H. Feldmeier, T. Neff, P. von Neumann-Cosel, and A. Richter. In: *Phys. Rev. Lett.* 98 (2007), p. 032501.

[Che18] Chemgas. `www.chemgas.com`. Accessed: 2018-07-16. 2018.

[Coo57] C. W. Cook, W. A. Fowler, C. C. Lauritsen, and T. Lauritsen. In: *Phys. Rev.* 107 (1957), pp. 508–515.

[Cry18] Saint Gobain Crystals. *Saint-Gobain Crystals*. 2018. URL: `https://www.crystals.saint-gobain.com/`.

[Dav63] R. H. Davis. "Proceedings of the Third Conference on Reaction between Complex Nuclei, Asilomar". In: (1963), p. 67.

[Don16] L. M. Donaldson. "Effect of deformation on the broad and fine structure of the Isovector Giant Dipole Resonance in $^{142-150}$Nd and ^{152}Sm". PhD thesis. University of the Witwatersrand, 2016.

[Ebr12] J. P. Ebran, E. Khan, T. Niksic, and D. Vretenar. In: *Letters to Nature* 487 (2012), p. 341.

[EXF98] Experimental Nuclear Reaction Data Library (EXFOR). In: *IAEA Nuclear Data Section. http://www-nds.iaea.org/exfor/* (1998).

[Fre09] M. Freer, H. Fujita, Z. Buthelezi, J. Carter, R. W. Fearick, S. V. Förtsch, R. Neveling, S. M. Perez, P. Papka, F. D. Smit, J. A. Swartz, and I. Usman. In: *Phys. Rev. C* 80 (2009), p. 041303.

[Fuj99] M. Fujiwara, H. Akimune, I. Daito, H. Fujimura, Y. Fujita, K. Hatanaka, H. Ikegami, I. Katayama, K. Nagayama, N. Matsuoka, S. Morinobu, T. Noro, M. Yoshimura, H. Sakaguchi, Y. Sakemi, A. Tamii, and M. Yosoi. In: *Nuclear Instruments and Methods in Physics Research Section A: Accelerators, Spectrometers, Detectors and Associated Equipment* 422.1 (1999), pp. 484–488.

[Fun03] Y. Funaki, A. Tohsaki, H. Horiuchi, P. Schuck, and G. Röpke. In: *Phys. Rev. C* 67 (2003), p. 051306.

[Fun05] Y. Funaki, A. Tohsaki, H. Horiuchi, P. Schuck, and G. Röpke. In: *Eur. Phys. J. A* 24 (2005), pp. 321–342.

[Fun06] Y. Funaki, A. Tohsaki, H. Horiuchi, P. Schuck, and G. Röpke. In: *Eur. Phys. J. A* 28 (2006), pp. 259–263.

[Fun07] Y. Funaki et al. In: *Nucl. Phys. News* 17 (2007), p. 11.

[Fun08] Y. Funaki, T. Yamada, H. Horiuchi, G. Röpke, P. Schuck, and A. Tohsaki. In: *Phys. Rev. Lett.* 101 (2008), p. 082502.

[Fun09] Y. Funaki, H. Horiuchi, W. von Oertzen, G. Röpke, and P. Schuck. In: *Phys. Rev. C* 80 (2009), p. 064326.

[Fun10] Y. Funaki, T. Yamada, A. Tohsaki, H. Horiuchi, G. Röpke, and P. Schuck. In: *Phys. Rev. C* 82 (2010), p. 024312.

[Fyn05] H. O. U. Fynbo. In: *Nature (London)* 433 (2005), p. 136.

[Gam28] G. Gamow. In: *Zeitschrift für Physik* 51 (1928), pp. 204–212.

[Gra95] A. Graps. In: *IEEE Comput. Sci. Eng.* 2 (1995).

[Hod78] P.E. Hodgson. "Nuclear heavy-ion reactions". In: (1978).

[Hor68] H. Horiuchi and K. Ikeda. In: *Prog. Theor. Phys.* 40 (1968), p. 277.

[Hoy54] F. Hoyle. In: *Astrophys. J. Suppl. Ser.* 1 (1954), p. 121.

[Ike68] K. Ikeda, N. Takigawa, and H. Horiuchi. In: *Suppl. Prog. Theor. Phys. Extra Number* 464 (1968).

[Ins18] Paul Sherrer Institute. *Maximum Integrated Data Acquisition System*. 2018 (accessed February 27, 2018). URL: `https://midas.triumf.ca`.

[Kam81] M. Kamimura. In: *Nucl. Phys. A* 351 (1981), p. 456.

[Kar95] S. Karataglidis, P. J. Dortmans, K. Amos, and R. de Swiniarski. In: *Phys. Rev. C* 52 (1995), p. 861.

[Kno00] G.F. Knoll. "Radiation Detection and Measurement". In: (2000).

[Kun13] P. D. Kunz. "Zero Range Distorted Wave Born Approximation". In: (2013). URL: `http://citeseerx.ist.psu.edu/viewdoc/download?doi=10.1.1.617.4863&rep=rep1&type=pdf`.

[Kun93] P.D. Kunz and E. Rost. "Distorted Wave Born Approximation". In: *Computational Nuclear Physics 2* (1993). URL: `https://link.springer.com/chapter/10.1007/978-14613-9335-1_5`.

[Li17] K. C. W. Li, R. Neveling, P. Adsley, P. Papka, F. D. Smit, J. W. Brümmer, C. Aa. Diget, M. Freer, M. N. Harakeh, Tz. Kokalova, F. Nemulodi, L. Pellegri, B. Rebeiro, J. A. Swartz, S. Triambak, J. J. van Zyl, and C. Wheldon. In: *Phys. Rev. C* 95 (2017), p. 031302.

[Mat75] T. Mathuse, M. Kamimura, and Y. Fukushima. In: *Prog. Theor. Phys.* 53 (1975), p. 706.

[Mer92] A. C. Merchant and W.D.M. Rae. In: *Nucl. Phys. A* 549 (1992), p. 431.

[MID19] MIDAS. *Maximum Integrated Data Acquisition System*. 2019 (accessed February 7, 2019). URL: `https://en.wikipedia.org/wiki/Maximum_Integrated_Data_Acquisition_System`.

[Myo14] T. Myo, A. Umeya, K. Horii, H. Toki, and K. Ikeda. In: *Progress of Theoretical and Experimental Physics* 3 (2014).

[Nak71] A. Nakada, Y. Torizuka, and Y. Horikawa. In: *Phys. Rev. Lett.* 27 (1971), p. 861.

[Nev11] R. Neveling, H. Fujita, F. D. Smit, T Adachi, G. P. A. Berg, E. Z. Buthelezi, J. Carter, J. L. Conradie, M. Couder, R. W. Fearick, S. V. Förtsch, D. T. Fourie, Y. Fujita, J. Görres, K. Hatanaka, M. Jingo, A. M. Krumbholz, C. O. Kureba, J. P. Mira, S. H. T. Murray, P. von Neumann-Cosel, S. O'Brien, P. Papka, I. Poltoratska, A. Richter, E. Sideras-Haddad, J. A. Swartz, A. Tamii, I. T. Usman, and J. J. van Zyl. In: *Nuclear Instrumentations and Methods in Physics Research A* 654 (2011), pp. 29–39.

[Nev17] R. Neveling, F. D. Smit, H. Fujita, P. Adsley, K. C. W. Li, J. W. Brummer, D. J. Marin–Lambarri, and R. T. Newman. "Guide to the K600 magnetic spectrometer". In: *Unpublished* (2017).

[Ohk10] S. Ohkubo and Y. Hirabayashi. In: *Phys. Lett. B* 684 (2010), p. 127.

[Ols73] David K. Olsen, Takeshi Udagawa, Taro Tamura, and Ronald E. Brown. In: *Phys. Rev. C* 8 (1973), pp. 609–620.

[ROO19] ROOT. *ROOT Data Analysis Framework*. 2019 (accessed February 7, 2019). URL: `https://root.cern.ch/`.

[Rot04] R. Roth, T. Neff, H. Hergert, and H. Feldmeier. In: *Nucl. Phys. A* 745 (2004), pp. 155–362.

[Sal52] E.E. Salpeter. In: *Astrophys. J.* 115 (1952), p. 326.

[Sat80] G.R. Satchler. "Introduction to Nuclear Reactions". In: (1980).

[Sat83] G.R. Satchler. "Direct Nuclear Reactions". In: (1983).

[She05] A. Shevchenko. "Fine structure of the Isoscalar Giant Quadrupole Resonance from High-Resolution Inelastic Proton Scattering Experiments". PhD thesis. T.U. Darmstadt, 2005.

[Spe81] R. H. Spear. In: *Phys. Rep.* 73 (1981), p. 369.

[Swa10] J. A Swartz. *A feasibily study of the (^{3}He,^{8}He) reaction with the K600 magnetic spectrometer. MSc thesis*. 2010.

[Swa14] J. A. Swartz. "Search for low-spin states above the 5-α break-up threshold in ^{20}Ne". PhD thesis. University of Stellenbosch, 2014.

[Swa15] J. A. Swartz, B. A. Brown, P. Papka, F. D. Smit, R. Neveling, E. Z. Buthelezi, S. V. Förtsch, M. Freer, Tz. Kokalova, J. P. Mira, F. Nemulodi, J. N. Orce, W. A. Richter, and G. F. Steyn. In: *Phys. Rev. C* 91 (2015), p. 034317.

[Swa17] J. A. Swartz, P. Adsley, B. A Brown, W. Brummer, H. O. U. Fynbo, O. S. Kirsebom, K.C.W. Li, D.J. Marin-Lambarri, M. Munch, F. Nemulodi, R. Neveling, P. Papka, L. Pellegri, V. Pesudo, W.A. Richter, F.D. Smit, S.M. Triambak, and J. J. Van Zyl. "Research proposal to the iThemba LABS: Physical Sciences Research programme on SSC facility". In: (2017).

[Tan74] F. Tanabe and F. Nemoto. In: *Prog. Theor. Phys.* 51 (1974), p. 2009.

[Toh01] A. Tohsaki, H. Horiuchi, P. Schuck, and G. Röpke. In: *Phys. Rev. Lett.* 87 (2001), p. 192501.

[Tor98] C. Torrence and G.P. Compo. In: *Bull. Am. Meteorol. Soc* 79 (1998), pp. 61–78.

[Weg87] H. E. Wegner. "Nuclear and Particle Physics Source Book". In: (1987). URL: https://www.amazon.co.uk/Nuclear-Particle-Physics-Science-Reference/dp/0070455090.

[Whe37] J. A. Wheeler. In: *Phys. Rev.* 52 (1937), pp. 1107–1122.

[Yam04] T. Yamada and P. Schuck. In: *Phys. Rev. C* 69 (2004), p. 024309.

[Yam05] T. Yamada and P. Schuck. In: *Eur. Phys. J. A* 26 (2005), p. 185.